



CHORUS

This is the accepted manuscript made available via CHORUS. The article has been published as:

Mass enhancement in MnO_3 and MnO_2 perovskites from symmetry breaking

Zhi Wang, Oleksandr I. Malyi, Xingang Zhao, and Alex Zunger

Phys. Rev. B **103**, 165110 — Published 9 April 2021

DOI: [10.1103/PhysRevB.103.165110](https://doi.org/10.1103/PhysRevB.103.165110)

Mass enhancement in 3d and s-p perovskites from symmetry breaking

Zhi Wang, Oleksandr I. Malyi, Xingang Zhao, and Alex Zunger

Renewable and Sustainable Energy Institute, University of Colorado, Boulder, Colorado 80309

Abstract

In some *d*-electron oxides the measured effective mass m_{exptl}^* has long been known to be significantly larger than the model effective mass m_{model}^* deduced from mean-field band theory, *i.e.*, $m_{\text{exptl}}^* = \beta m_{\text{model}}^*$, where $\beta > 1$ is the “mass enhancement”, or “mass renormalization” factor. Previous applications of density functional theory (DFT), based on a *symmetry-restricted* structure with the smallest number of possible magnetic, orbital, and structural degrees of freedom, missed such mass enhancement. This fact has been taken as evidence of strong electronic correlation, often described via symmetry-restricted, dynamic mean-field approach of many-body theory, being the *exclusive* enabling physics. The present paper uses instead a static density functional approach that does not restrict positional or spin degrees of freedom (symmetry-broken structures). It analyzes the contributions of different symmetry-broken modalities to mass enhancement, in the range of the nominally highly correlated *d*-electron perovskites, as well as the nominally uncorrelated, closed-shell *s-p* bonding perovskites. It shows that the energy-lowering symmetry-broken spin effects (*e.g.*, nonzero local moment) and structural effects (*e.g.*, atomic displacement) as described in mean-field DFT, manifests already mass enhancement for both electrons and holes in a range of *d*-electron perovskites SrVO₃, SrTiO₃, BaTiO₃, and LaMnO₃, as well as *p*-electron perovskites CsPbI₃ and SrBiO₃, including both metals (SrVO₃) and insulators (the rest). This is revealed only when enlarged unit cells of the same parent global symmetry, which are large enough to allow for symmetry breaking distortions and concomitant variations in spin order, are explored for their ability to lower the total energy. *Positional* symmetry breaking that lead to mass enhancement include octahedral rotation in halide perovskites such as CsPbI₃, Jahn-Teller-like Q_2^+ distortion in LaMnO₃, and bond disproportionation in SrBiO₃, while *magnetic* symmetry breaking resulting in mass enhancement include the formation of a distribution of local moments in SrVO₃ that averages to zero in the paramagnetic phase. Not all symmetry breaking lead to significant mass enhancement, *e.g.*, the rather small octahedral rotations in the nearly perfectly cubic SrTiO₃ cause but negligible mass enhancement, so do the paraelectric displacements in BaTiO₃. In *principle*, by ergodicity, the two descriptions, *i.e.*, the symmetry-restricted dynamic approach with a single time-fluctuating magnetic moment, and the symmetry-broken mean-field approach with a static distribution of spatially fluctuated local moments, are not

mutually exclusive, but a choice of representation (and consequently a choice of computational efficiency), at least if both approaches are carried out exactly. In *approximate implementations*, symmetry-broken mean-field approach appears to remove much of what was strong correlation in dynamically correlated symmetry-restricted solutions, leaving smaller ('weak') residual correlation with respect to the exact solution.

I. Introduction

The effective mass m^* defined [1] as the reciprocal of the wave vector curvature $\partial^2 E / \hbar^2 \partial k_i \partial k_j$ of the band dispersion relation $E(k)$ (where k_i and k_j are wave vectors) is a central quantity in condensed matter physics, widely used to characterize the band structure, carrier transport, and wave function localization. Recently, this quantity has attracted attention in the context of d -electron correlated oxide physics, where the measured effective mass m_{exptl}^* has been noted in some cases to be significantly larger than the model effective mass m_{model}^* deduced from simplified mean-field band theory, $m_{\text{exptl}}^* = \beta m_{\text{model}}^*$, where β is the ‘mass enhancement’, or ‘mass renormalization’ factor. Here, m_{exptl}^* are generally deduced from experiment via model assumptions (such as band parabolicity or various averages over the mass tensor), leading to different effective mass definitions in different experiments, including the mass deduced from Fermi-velocity (v_F) as $m^* \propto 1/v_F$, from density of states (DOS) $m^* \propto (D(E))^{2/3}$, from specific-heat coefficient $m^* \propto \gamma$, from magnetic susceptibility $\chi \propto m^* \left(1 - \frac{m_0^2}{3m^{*2}}\right)$, and from the band width $W \propto 1/m^*$. Values of $\beta > 1$ were reported in the literature for Fe-based superconductors [2,3], halide perovskites [4], titanites [5–7], ruthenates [8–10], and vanadates [11–14], *etc.* These mass enhancement factors from experiment $\beta(\text{exptl}/\text{model}) = m_{\text{exptl}}^*/m_{\text{model}}^*$ were then compared with the theoretical values $\beta(\text{Theory}/\text{model}) = m_{\text{Theory}}^*/m_{\text{model}}^*$ obtained from many-body approaches (such as dynamic mean-field theory, DMFT [15–24]). Because m_{model}^* comes from the mean-field band theory, the predicted theoretical enhancement $\beta(\text{Theory}/\text{model}) > 1$ has been interpreted to be due to strong correlation effects [15–24]. For example, in DMFT, wavefunction localizes and bandwidth narrows (thus leading to mass enhancement) due to pure *electronic* symmetry breaking [24,25] induced by the dynamic self-energy from the impurity atom embedded in a mean-field bath. Finding for a compound that $\beta(\text{DMFT}/\text{model}) > 1$ consistent with $\beta(\text{exptl}/\text{model}) > 1$ helped classify the pertinent compounds as being highly correlated, given that mean-field theory has been argued unable to describe the mass enhancement.

This line of thinking, however, does not consider the possibility that mass enhancement could be described by methods other than using symmetry-restricted structures. Indeed, the model calculations used to extract m_{model}^* have invariably been [15–24] rather naive (N) level of density functional theory (N-DFT), based on symmetry-restricted structures with the least number of possible magnetic, orbital, and structural degrees of freedom. Such calculations have assumed one or a few of the following approximations: A highly symmetric unit cell (*e.g.*, $\text{Pm}\bar{3}\text{m}$ cubic containing only a single formula unit), no atomic displacements relative to the averaged

high symmetry structure, and/or a nonmagnetic (NM) spin configuration. The shortcomings of such simplistic N-DFT approaches are evident among others in (i) predicting *metallic states* for known insulators (as illustrated for binary 3d NiO, MnO, CoO and FeO insulators [26], ternary 3d oxide perovskites [27] LaVO₃, LaMnO₃ and YNiO₃, as well as other compounds [28,29] such as CaIrO₃, LaTiO₃, SrBiO₃, TiO_{2-x}, CeO_{2-x}, CuBi₂O₄, Sr₂IrO₄, Li_xTiO₂ and Ba₄As₃), and by the fact that (ii) they predict a total energy far higher (by ~1 eV per formula unit, eV/f.u.) than what conventional DFT [27] provides, as well as by (iii) missing the orbital order [27].

The failures of these naïve applications of mean-field band theory to predict electronic properties often go hand in hand with the assumption of the symmetry-restricted structure. For example, the cubic crystal structure of *halide perovskites* ABX₃ (A = Cs, MA, FA; B = Sn, Pb; X = Cl, Br, I) is described in X-ray diffraction databases as Pm $\bar{3}$ m cubic, having a single ABX₃ formula unit, with all octahedra being ideally shaped, untitled, and oriented parallel to each other, representing a single BX₆ local motif (monomorphous structure). This Pm $\bar{3}$ m cubic structure has been extensively used [30–33] to calculate the standard electronic band structure as well as phonon lattice dynamics. However, in reality, the cubic phase of such ABX₃ perovskites often manifests *static* atomic distortions off Wyckoff positions as an intrinsic expression of their chemical bonding, as seen by local probes [34,35] and reproduced by static total energy optimization [36], even before the contribution of thermal motion sets in. Whereas these symmetry breaking are observable from X-ray local probe measurements, *e.g.*, the extended X-ray-absorption fine-structure (EXAFS) and pair distribution function (PDF) [37–42], these symmetry breaking are easy to miss in DFT if one uses the *average* X-ray diffraction (XRD) Pm $\bar{3}$ m cubic cell, because that such a single cell geometrically excludes the creation of a periodic lattice with tilted octahedra. Permitting a larger cell (“supercell”) yet with constrained cubic lattice vectors provides the geometrical freedom to distort octahedra. Similarly, there are reasons to suspect that this simpler symmetry breaking physics, positional as well as magnetic (both sanctioned by single-determinant mean-field band theory view), could also affect the effective mass. For example, oxide perovskites are known to manifest octahedral rotations and tilting [43], displacements [44], bond disproportionation [45], and Jahn-Teller distortions [46], while such local modes can couple to the electronic structure, leading to shifted band energies [30,47–52], thus possibly leading to mass renormalization. Also, whereas the PM phases in 3d oxides were once treated as NM [12–18] [53–55] (thus, interpreting the zero global magnetic moment as being zero on an atom-by-atom basis), more recent theories allowed for the existence of a *distribution* of different spin environments adding up to zero, constitutes a *polymorphous network* that couples to electronic properties [36,56–58]. The existence of a distribution of positional as well as local magnetic environments needs to be investigated for its ability to affect the band structure and hence the effective masses.

Therefore, instead of leapfrogging from N-DFT to dynamically correlated methods such as DMFT, it would seem informative to retain the m_{model}^* mass but replace m_{Theory}^* in $\beta(\text{Theory/model}) = m_{\text{Theory}}^*/m_{\text{model}}^*$ by mean-field theory that allows for possible magnetic, orbital, and structural degrees of freedom, which could break symmetries while lowering the total energy. It can be done by using DFT that is free from oversimplified symmetry-restricted approximations which are not an essential part of DFT. This $\beta(\text{DFT/N-DFT}) = m_{\text{DFT}}^*/m_{\text{N-DFT}}^*$ might include many symmetry-broken effects routinely included in contemporary DFT calculations, such as (i) *positional symmetry breaking*, e.g., octahedral rotations, Jahn-Teller distortions, and bond disproportionation, all observed experimentally, and (ii) *magnetic symmetry breaking*, e.g., allowing spin configurations such as antiferromagnetic (AFM) and paramagnetic (PM) rather than the NM approximation. Effective allowance for (i) and (ii) also necessitates the use of exchange-correlation functionals that produce correctly compact orbitals (due to closer adherence to the generalized Koopmans condition [59]) but not an overestimated orbital localization (such as in the Hartree-Fock functional).

That symmetry breaking in approximate mean-field theory could capture events that in restricted symmetric structures would require a complex correlated treatment, has been amply illustrated in molecular systems. For example, as pointed out in 1972 by Bagus and Schaefer [60], describing a core hole state in diatomic O_2 while retaining the high $D_{\infty h}$ symmetry is made computationally difficult by the extreme complexity of packing the electron-electron pair correlation into a small, symmetric space. Yet breaking molecular orbital symmetry by placing the hole initially on a single atom in Hartree-Fock calculation agrees well with the experiment. In principle, by ergodicity, the two descriptions, i.e., (a) the symmetry-restricted dynamic approach with a single *time-fluctuating* magnetic moment, vs. (b) the symmetry-broken mean-field approach with *spatially fluctuated* local moments, are not mutually exclusive, but are a choice of representation, and consequently a choice of computational efficiency, at least if both approaches are carried out exactly. In the *exact implementations*, (a) dynamic symmetry-restricted and (b) static symmetry-broken ground states should have the same ground state energies [59–63]. In approximate implementations, experience in a two-center molecular system (such as stretched H_2 , Li_2 , or O_2) indicated that, symmetry-broken mean field removes much of what was strong correlation in symmetry-restricted, dynamically correlated solutions, leaving smaller ('weak') residual correlation with respect to the exact solution. Thus, a correlation that has been dynamic in the symmetry-restricted case can become static in the symmetry-broken cases, and the correlated methods in symmetry-restricted structures might not be the only way to describe mass enhancement [63]. Symmetry can be restored afterward [64] and often gives for localized states but small additional energy lowering. A review of the

traditional role of symmetry-broken mean field vis-à-vis symmetry-restricted correlation and that these are non-additive effects has been recently presented by Perdew *et al.* [63]

Such symmetry-broken mean-field approach can furthermore provide clear intuition as to the mechanism whereby the electronic structure (here, mass enhancement) is established. The classic picture of the face-centered cubic “empty lattice” band structure, having but the symmetry of primitive cell without interactions, as illustrated by F. Herman in 1958 [65], shows broad bands and high degeneracies with low masses. Any successive introduction of interaction terms into this empty lattice Hamiltonian (starting with the point-ion pseudopotential) would progressively remove band degeneracies, split broad bands into sets of sub-bands, and lead to mass enhancement. Examples of known modalities of symmetry breaking that are now shown to lead specifically to mass enhancement are summarized in Fig. 1 and discussed in the following sections. We find that indeed these energy-lowering, mean-field, symmetry-broken modalities (lines 2-6) can enlarge the band gap and/or contribute to more localized wavefunctions, thus leading to mass enhancements, not only for electrons but also for holes, which were previously attributed exclusively to explicitly correlated methodologies.


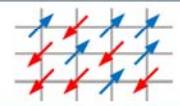
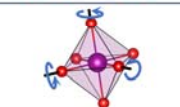
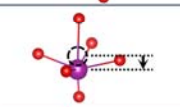
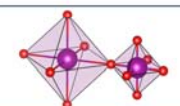
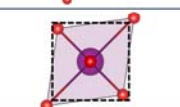
Modality		Symmetry breaking degree of freedom	Schematic	Example in this work
(a) Strong electronic correlation		Electronic symmetry breaking		
(b) Magnetic symmetry breaking		Different local spin configurations		SrVO ₃ (PM cubic)
Positional symmetry breaking	(c) Octahedral rotation	Rotation angles		CsPbI ₃ , SrTiO ₃ (NM cubic)
	(d) Atom displacement	Local polarizations		BaTiO ₃ (AFE cubic)
	(e) Bond disproportionation	Different octahedral volumes		SrBiO ₃ (NM monoclinic)
	(f) Jahn-Teller distortion	Inequivalent bond lengths		LaMnO ₃ (AFM orthorhombic)

Figure 1 (1.5 columns) | Modalities of symmetry breaking illustrated for the perovskite structure. From top to bottom: (a) Strong electronic correlation as schematically shown by the Hubbard model; (b) magnetic symmetry breaking such as the paramagnetism (PM), where the lattice sites are occupied by atoms having opposite spins without long-range order; (c)

octahedral rotations allowing non-zero rotation angles; (d) atomic displacements such as the ferroelectric displacements in perovskites inducing a local polarization degree of freedom; (e) bond disproportionation allowing octahedra in perovskites to have different volumes; (f) Jahn-Teller distortions elongating the perovskite octahedron along one direction, leading to inequivalent bond lengths between the center and corner atoms.

The intuition behind this investigation originates from that the factors that effective masses can be gleaned qualitatively from $\mathbf{k} \cdot \mathbf{p}$ perturbation theory [66],

$$\frac{1}{m_{n_j}^*} = \frac{1}{m_0} + \frac{2}{m_0^2 k^2} \left(\sum_{l \notin \{n\}} \frac{|\langle n\mathbf{0} | \mathbf{k} \cdot \mathbf{p} | l\mathbf{0} \rangle|^2}{E_{n0} - E_{l0}} + \epsilon_{n_j, \mathbf{k}} \right) \#(1)$$

where $m_{n_j}^*$ is the effective mass of state $|n_j, \mathbf{0}\rangle$ at band edge, $\mathbf{0}$ denotes the momentum where the band edge is located, subscript j is the index of degenerated wave functions, m_0 is the free-electron mass, $E_{n0} - E_{l0}$ are inter-band energy gaps, and $\epsilon_{n_j, \mathbf{k}}$ are the energy shifts from band degeneracy (zero if no degeneracy). The sum is over all eigenstates $|l\mathbf{0}\rangle$. This classic expression teaches that the effective mass in solids is generally enhanced by any effects that increase the inter-band energy gaps $\{E_{n0} - E_{l0}\}$ and/or reduce the wavefunction momentum matrix element $\langle n\mathbf{0} | \mathbf{k} \cdot \mathbf{p} | l\mathbf{0} \rangle$, *i.e.*, producing more compact wavefunctions.

In the present paper, we use the textbook definition of the effective mass m^* as the reciprocal of the wave vector curvature $\partial^2 E / \hbar^2 \partial k_i \partial k_j$, except that instead of insisting on an electronic structure based on symmetry-restricted primitive unit cell, we allow a larger, symmetry-broken cell. While there is no ‘theorem’, to our knowledge, showing if DFT can describe exactly band energies thus effective masses, our justification and indeed method of analysis rely on the insight (but not literal details) from this $\mathbf{k} \cdot \mathbf{p}$ theorem (Eq.1), indicating how effective masses are related to band gap. The fact that effective masses are often evaluated from band widths in DFT and in many-body calculations (as implied in previous DMFT [15–24]), as well as in experimental literature [2,3,6,13,14] supports this tradition. Note that the DFT band gap is described as the *total-energy difference gap*, *i.e.*, the difference between ionization potential $I = E(M - 1) - E(M)$ and the electron affinity energy $A = E(M) - E(M + 1)$ where M is the number of electrons. Such a total-energy difference gap is a proxy to the quasiparticle gap. Since, in this definition, only the ground-state energies are involved, this total-energy difference gap can be calculated, in principle exactly from DFT, and can be directly compared to that measured from experiments [67–69]. Now, the quantity that is practically calculated often is the single-particle band gap $E_{CBM} - E_{VBM}$. Ref [69] has shown that such single-particle gap is equal to the

total-energy difference band gap for the same exchange-correlation (XC) functional, if the XC is a non-multiplicative potential (operator is continuous) and the density change is delocalized when an electron or hole is added. This applies to LSDA, PBE, SCAN, and hybrid functionals. The following sections III and IV will provide the different definitions of effective mass that have been examined. The present DFT results with symmetry breaking and no dynamic correlation show comparable masses to DMFT and experimental data.

Table I lists mass enhancements calculated by symmetry-broken mean-field DFT in the present paper for six compounds, compared with experimental observations previously reported for SrVO₃, CsPbI₃, LaMnO₃, and SrTiO₃. Previous DMFT calculations for SrVO₃, LaMnO₃, and SrTiO₃ are also given in Table I. Many of the mass enhancements found by symmetry-broken DFT here are comparable in magnitude to the values suggested by the correlated methods. We see that mass enhancement by symmetry-broken DFT is not unique to open-shell *d*-electron compounds, and similar magnitudes of mass enhancements also exist for *s-p*-bonding compounds. This further suggests that viewing the presence of mass enhancement in the considered compounds as evidence for the exclusive need for strong dynamically correlated methodologies [15–24], is not a safe practice before examining the effect of positional and magnetic symmetry-broken effects on the band structure.

Table I | Summary of mass enhancement factors β_e for electron and β_h for hole, compared with experimental observations and DMFT calculations, for the compounds investigated in this work. We provide (i) the observed low-temperature low-symmetry ground states, (ii) the phases studied in this work for which mass enhancements were reported in the literature, (iii) the symmetry-restricted models used in the literature by DFT and DMFT, (iv) the symmetry-broken modes found presently by DFT in the phases studied, and (v) the mass enhancements found in this work. Magnetic orders NM, AFM and PM denote nonmagnetic, antiferromagnetic and paramagnetic, respectively. Here several different DMFT values are given for comparison, because the DMFT calculated mass enhancement depends on the U value and the method to remove the double-counting potential. For cubic CsPbI₃, to the best of our knowledge, there are no experimental reports for separate electron and hole masses, and only reduced mass $m_r^* = -m_e^*m_h^*/(m_e^* + m_h^*)$ has been reported for CsPbBr₂ [70]; our result is therefore compared with such experimental reduced mass.

Compound	Ground state	Phase studied in this work	Symmetry-restricted model (ref. $\beta=1$)	Symmetry-broken mode found by DFT	Mass enhancement
SrVO ₃	PM cubic	PM cubic	NM $Pm\bar{3}m$	Magnetic symmetry breaking	β_e DFT: 1.5±0.1, (exp.: 1.3 ^b , 2.2 ^c , 2.9 ^c , DMFT: 1.8±0.2 ^a)
					β_h DFT: 1, (exp.: 1 ^d)
CsPbI ₃	NM orthorhombic	NM cubic	NM $Pm\bar{3}m$	Octahedral rotation	β_e DFT: 1.8 [†] , (exp.: $m^*=0.12m_0$ [†])
					β_h DFT: 2.2 [†] , (exp.: $m^*=0.12m_0$ [†])
LaMnO ₃	AFM orthorhombic	AFM orthorhombic	AFM $Pnma$ (no Jahn-Teller)	Jahn-Teller distortion	β_e DFT: 1.8±0.5
					β_h DFT: 1.6±0.4, (exp.: 2.6-2.8 ^e , DMFT: 1.3-1.7 ^f)
SrBiO ₃	NM monoclinic	NM monoclinic	NM $P2_1/n$ (no disproportionation)	Bond disproportionation	β_e DFT: 1.3±0.2
					β_h DFT: 1.5±0.2
SrTiO ₃	NM tetragonal	NM cubic	NM $Pm\bar{3}m$	Octahedral rotation	β_e DFT: 1.1, (exp.: 2-3 ^g , DMFT: 1 ^g)
					β_h DFT: 1.1
BaTiO ₃	NM rhombohedral	NM cubic	NM $Pm\bar{3}m$	Ferroelectric displacement	β_e DFT: 1.1
					β_h DFT: 1

[†] DFT calculated reduced mass $m^*=0.14m_0$, and experimentally measured reduced mass (for cubic CsPbBr₂) $m^*=0.12m_0$ [70].

[a] Reference [11,12,14]; [b] reference [16]; [c] reference [17]; [d] estimated from reference [71]; [e] reference [72]; [f] by comparing this work with reference [53]; [g] reference [73].

II. Approach

Supercell model. To allow for inclusion of the pertinent symmetry-lowering effects, the tradition of using the most economical minimal unit cell must be avoided because it might geometrically disallow symmetry breaking. Instead, one should use a $N_1 \times N_2 \times N_3$ replica of such minimal cell (*i.e.*, a supercell). Table I shows for each compound (i) the observed low-symmetric ground state at low temperature, (ii) the mass-enhanced phase studied in this work, (iii) the symmetry-restricted minimal-cell model previously used in the literature. We see that the structure for which mass enhancement was reported in the experiment and studied in previous DMFT calculation is not always the ground-state structure, *e.g.*, for halide perovskites such as CsPbI₃ and oxide perovskite SrTiO₃, the ground states are orthorhombic and tetragonal, respectively, while it is the cubic phase where mass enhancements were reported [4,73]. In such cases where the phase studied is not the ground-state phase, the supercell model is constrained throughout the calculation to have the global lattice symmetry of the phase *studied* (*e.g.*, cubic), but all internal atomic positions are allowed to attain the values that minimize the (constrained) total energy. To assure that the relaxed atomic positions are reliable (*e.g.*, not saddle points on the potential surface), all atoms have been initially ‘nudged’ by applying random atomic displacements (random for both direction and amplitude), prior to starting the process of following total-energy minimization. The size of the supercell is increased until convergence on total energy is found; the cell size is not directly important *per se* except that certain cells cannot, by symmetry, allow symmetry breaking even if it will lower the energy. This dependence of total energy per atom on the cell size is unique to certain (polymorphous network) compounds but not in conventional materials, such as silicon or ZnSe, where it does not show different total energies between supercell and minimal-cell model. Thus, larger than minimal (super) cells do not necessarily lead to disorder or mass enhancement unless energy lowering takes place.

In all magnetic calculations, the *directions* of spin moment on every site are collinear and fixed (*i.e.*, spin flip is not allowed), while the *amplitudes* of magnetic moment are free to evolve during the total energy minimization. In principle, spins can relax during the electron self-consistency calculations to produce non-random configurations. We have confirmed that our DFT self-consistent calculations give negligible net magnetization for all AFM and PM structures (<0.001 Bohr magneton per atom).

Band unfolding. Whereas the supercell approach has the advantage of allowing the incorporation of local structural and spin motifs, it has the disadvantage of producing a non-intuitive and difficult-to-analyze dense band structure in the small reciprocal-space Brillouin zone (BZ) associated with the large real-space cell dimensions. This difficulty is overcome by applying rigorous band unfolding [74–76] to the supercell band structure, producing “effective band structures” (EBS) that replace the sharp bands of ordinary band theory by spectral functions (including both coherent and incoherent components).

Calculation of effective mass. We apply four models to calculate the mass and mass enhancement. (1) Deducing the mass from the mass tensor of the reciprocal for the second derivative of E vs \mathbf{k} at the band edges; if the mass tensor is anisotropic ($m_1^* \neq m_2^* \neq m_3^*$), the result mass will be calculated as $m^* = (1/m_1^* + 1/m_2^* + 1/m_3^*)^{-1}$. (2) Deducing the mass from the DOS at Fermi level $m^* \propto (D(E_F))^{2/3}$. (3) Deducing the mass from the slope of bands at Fermi level, *i.e.*, the Fermi velocity (v_F), as $m^* \propto 1/v_F$. (4) Deducing the mass from the bandwidth $m^* \propto 1/W$. Note that method (1) can give the absolute mass, while methods (2)-(4) are used only for the relative mass enhancement factor $\beta = m_{\text{Theory}}^*/m_{\text{model}}^*$, but not the absolute mass. We focus here on the mass enhancement factors (relative masses) rather than on the absolute value of masses.

III. Magnetic polymorphous network in paramagnets leads to mass enhancement: SrVO₃

Representation of the PM phase as a distribution of local spin environment. All calculations reported here are spin-polarized, allowing up and down spins. In addition, we allow for spatial spin symmetry breaking: the PM phases of 3d oxides are often described in the DFT literature as being *nonmagnetic*, interpreting the PM condition of globally-zero moment on an atom-by-atom basis, deducing that each atom must be nonmagnetic [12–18] [53–55]. This strong restriction does not follow from the definition of PM or from the DFT, and as was recently recognized, it leads to rather high total energy [27]. A correct description of PM entails allowing a larger (super) cell that can accommodate different local spin environments, should they lower the total (DFT) energy. For example, in a PM crystal where each magnetic ion is locally coordinated by N other magnetic ions, one can have in the collinear description a distribution of local spin environments, *e.g.*, an up-spin ion can be coordinated by $(N - m)$ up-spin ions plus m down-spin ions, where $0 \leq m \leq N$; if the up and down orientations are chosen randomly (which corresponds to the high-temperature limit of PM phase), it follows the Binomial statistics, *i.e.*, finding an ion with m down-spin neighbors follows the probability function

$P(m; N, 0.5) = \binom{N}{m} 0.5^N$. This model of PM local order represents a generalization of the AFM spin configuration that includes but a single local environment (*e.g.*, up-spin site coordinated only by down-spin sites), whereas, in the PM phase, the above noted additional local environments could exist. This is accomplished in practice by borrowing an idea known from the theory of substitutional A_xB_{1-x} alloys [77]: Construct an M -atom supercell for composition x with sites occupied by A-type and B-type atoms (here, up-spin and down-spin atoms), so that the atom-atom correlation function will mimic for a finite supercell a given statistic for the infinite cell (here, random Binomial statistics) the best possible way for a M -atom supercell. Such “Special Quasirandom Structures” (SQS’s) identify the most economical supercells for given size M . We currently use the *random* spin-spin correlation (corresponding to the high-temperature limit), although the use of non-random short-range order in SQS is possible [78,79].

We consider next the PM phase of SrVO₃ modeled by a 128-f.u. supercell (*i.e.*, 640 atoms per cell) with collinear up and down spin configuration. Figure 2b shows in red the distribution of DFT calculated up-spin and down-spin magnetic moments, whereas the single vertical blue line shows the all-site-having-zero-spin condition in the minimal-cell NM case. For all relaxed SrVO₃ supercells, we have found negligible atomic displacement, consistent with the fact that the size mismatch factor revealed by the Goldschmidt factor is negligible. Comparing different spin configurations including FM, AFM, and PM phases in SrVO₃ (Table II in Appendix B) shows nearly degenerate total energy, suggesting that the spin ground state could be a mixture of many possible magnetic orders, *i.e.*, in agreement with experiment [80,81] that SrVO₃ is a PM metal down to low temperatures and does not form magnetic order. Note that all magnetic phases show significant energy lowering when compared to the conventional NM model.

Electron mass enhancement in SrVO₃. Figure 2a shows the N-DFT band structure (cubic unit cell containing a single f.u., no relaxation, with NM spin configuration having zero moments at all sites) giving a metallic phase, with a conduction bandwidth of 2.5 eV. This model was used for m_{model}^* in many previous studies [12–17] to calculate mass enhancement using, *e.g.*, DMFT and GW theories. Figure 2c shows the spectral functions calculated in DFT from such 640-atom supercell, unfolded into the primitive BZ of SrVO₃. The unfolding procedure used in Figure 2c allows one to reduce the band structure complexity of a supercell, converting the sharp bands from the monomorphous case to an effective band structure having a finite band spread that depends on the distribution function used to describe the spin in PM supercell (in the current case we neglect the spin-spin short-range order, so the fuzziness may be overestimated). Figure 3 shows the evolution of the unfolded band structure as the real space supercell size increases, finding convergence.

SrVO₃ (paramagnetic cubic phase, PBE+U)

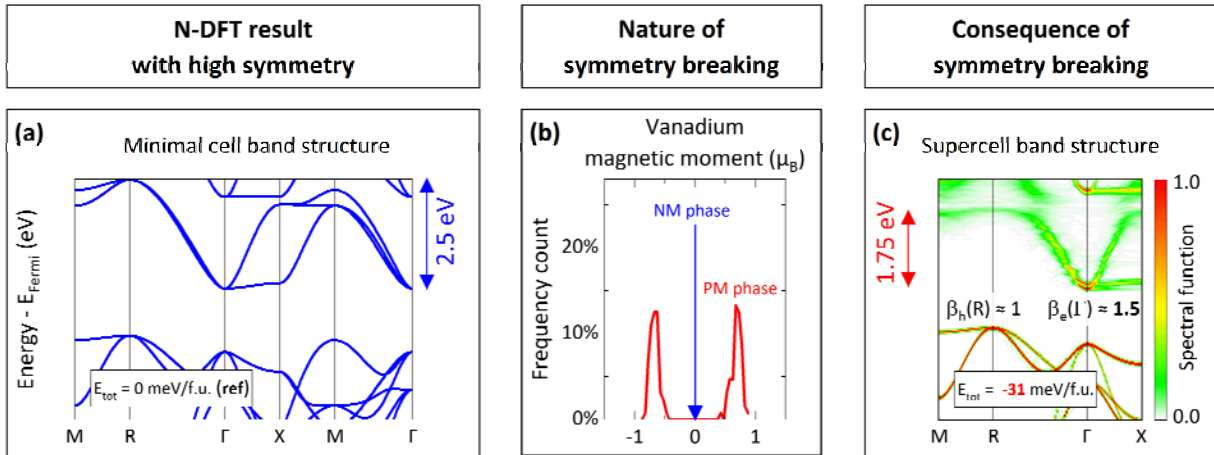


Figure 2 (2 columns) | Mass enhancements in the PM cubic phase of SrVO₃. (a) The band structure obtained from the same N-DFT restriction as in previous literature [12–18], namely a single-cell, cubic, NM SrVO₃ model using PBE+U (U=1.25 eV on V-d orbitals). (b) shows the distribution of spin moments in the present PM phase: Blue lines show that in the minimal-cell NM phase, all vanadium sites have zero magnetic moment, while the red curve shows that in the PM phase different vanadium sites have a distribution of different, non-zero magnetization. (c) shows the unfolded band structure when removing the minimal-cell restrictions by using instead a cubic, 128-fu PM supercell SrVO₃ with the same PBE+U method. Masses in (c) are calculated via DOS at Fermi level (which gives $\beta_h \approx 1.4$ -1.6 and $\beta_e = 1$; the subscript *e* and *h* denote the electron and hole mass enhancements; uncertainty is due to the variation of DOS nearby the Fermi level), second derivative of *E* vs *k* (which gives $\beta_h = 1.46$ and $\beta_e = 1$), and bandwidth (which gives $\beta_h = 1.43$ and $\beta_e = 1$). The vertical arrows in (a) and (c) show the bandwidths. The same PBE+U method has been applied for all SrVO₃ calculations.

The significant result is that the conduction band in the PM phase, allowed to have a distribution of local spin motifs, is narrowed relative to the minimal-cell NM case, from the 2.5 eV (Figure 2a) to 1.75 eV (Figure 2c). This leads to electron mass enhancement factor (β_e) in the PM supercell $\beta_e = 1.43$. Note that different definitions of effective mass give somewhat different results: The bandwidth mass enhancement of 1.43 can be compared with the density-of-states mass enhancement 1.4-1.6 at Fermi level, while the second derivative of *E* vs *k* at the conduction band edge gives 1.46. Note that we have not attempted to fit the result by adjusting *U*, although the choice of more localizing XC functional can increase the enhancement factor. We note that whereas the values obtained depend somewhat on the definition of effective mass used, the lattice constant (here we used $a=3.83$ Å), and the *U* value, allowing for polymorphous spin configuration, leads in all cases to an enhancement factor of 1.5 ± 0.1 . These calculated mass enhancements are comparable to the

experimentally measured factor $\beta_e(\text{exptl/N-DFT}) \approx 1.8 \pm 0.2$ [11,12,14], while smaller than the enhancement factors from DMFT, *e.g.*, $\beta_e(\text{DMFT/N-DFT}) = 2.9$ [17] (using a much larger $U = 5.5$ eV that narrows bands further) and from GW+DMFT $\beta_e = 1.3$ [16], 2.2 [17] (where the two values correspond to different versions of accounting approximately for the double-counting error in GW+DMFT).

Hole mass enhancement in SrVO₃. The DFT calculations naturally provide all bands with equal approximations, in particular, both the electron conduction band (mainly V-*d* orbitals) and the valence hole band (mainly O-*p* orbitals). We find no mass enhancement for hole states in the principal valence band, consistent with the fact that the spin configuration in the O *p*-like principal valence band corresponds to a closed electronic shell and negligible magnetic moment that show no distribution of motifs. We will see later that in ABX₃ perovskites, where the local environment is made of a distribution of *positional* motifs rather than from spin motifs, there will be both electron and hole mass enhancements.

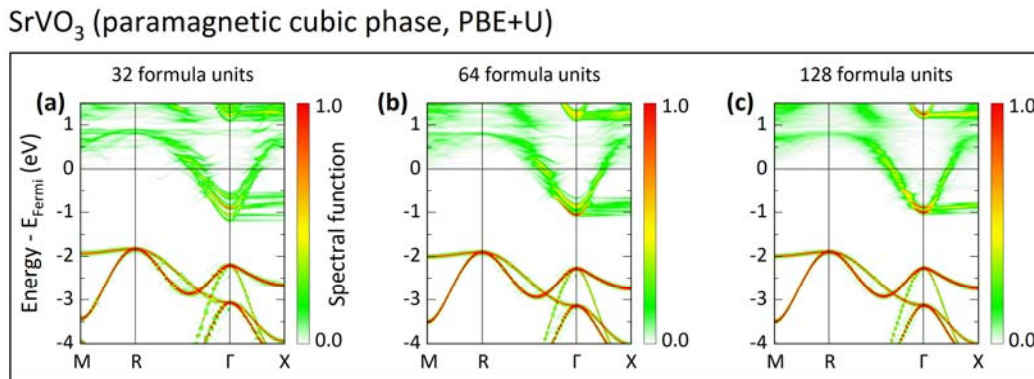


Figure 3 (2 columns) | Convergence of mass enhancement and band structure of SrVO₃ PM vs. supercell size increasing from 32 formula units (160 atoms), to 64 f.u. (320 atoms), to 128 f.u. (640 atoms). All supercells are generated by using the spin SQS method. Note band narrowing convergence.

Analysis of the contributing factors to spin-induced mass enhancement in SrVO₃. The real-space symmetry-broken supercell approach provides for an intuitive understanding of the results. The degree of freedom within our PM supercell is the local spin configuration (as we have found that the positional relaxation is negligible in this system). A local spin motif consists at the first order of a central 3*d* atom and its first-shell 3*d* (next nearest) neighbors. Whereas in the case of the minimal-cell NM model, each and every motif has zero spin, and in the case of AFM order, each motif has maximum dissimilarity between the spin of the central atom and the spins of its coordination shell (*e.g.*, the AFM-G like local motif when the central atom is up-spin, while all

its neighbors are all down-spin), in our model of the PM phase, each spin can have a local distribution of spins, including the case of maximum similarity (*e.g.*, the FM-like local spin motif when the central atom is up-spin, and so are all its neighbors), maximum dissimilarity, or any configurations in between. Figure 4(a)-(c) shows the *random* (high-temperature limit) statistical weight for each spin motif. Each local spin motif might have its unique, projected local density of states. The vertical arrows in Figure 4(d-i) indicate that each local spin motif contributes differently to the conduction bandwidth, whereas the reference minimal-cell result using the NM model (shown in Figure 4(d)) has considerably wider DOS. Figure 4(e-i) shows that the locally AFM-G-like vanadium sites with max spin dissimilarity with their neighbors have the most *compressed* DOS (Figure 4(i); smallest range in energy and the highest peak in DOS, indicating enhanced electron mass), while the locally FM-like sites with max spin similarity with the neighbors have the most *expanded* DOS (Figure 4(e); similar to the bandwidth in the NM model in Figure 4(d), hence not contributing to mass enhancement). Figure 4 suggests that the mass enhancement depends on spin short-range order (SRO), *i.e.*, the spin configuration at the center site and the neighbors, through the statistical weight for each spin motif (Figure 4b): an AFM-like, anti-clustering SRO can lead to a larger enhancement coefficient β , while a FM-like, clustering SRO can reduce β . This analysis teaches that the existence of a polymorphous distribution of spin-polarization motifs with their attendant, different local density of states contributing differently to the total DOS creates the possibility of *spin-induced mass enhancement*.

As discussed above, static DFT calculations permitting symmetry breaking and ensuing creation of local spin motifs naturally show mass enhancement. The scope of the current calculation of E-vs-k dispersion does not extend, however, to fully model ARPES spectra, including ARPES matrix element effects [82,83], or lifetime effects [84,85] associated with the observed sharpening of the ARPES states as they approach the Fermi level [12–14]. Description of lifetime-broadening generally requires a time-dependent dynamics analysis, *e.g.*, spin dynamics combined with molecular dynamics, possible in the mean-field DFT framework [86].

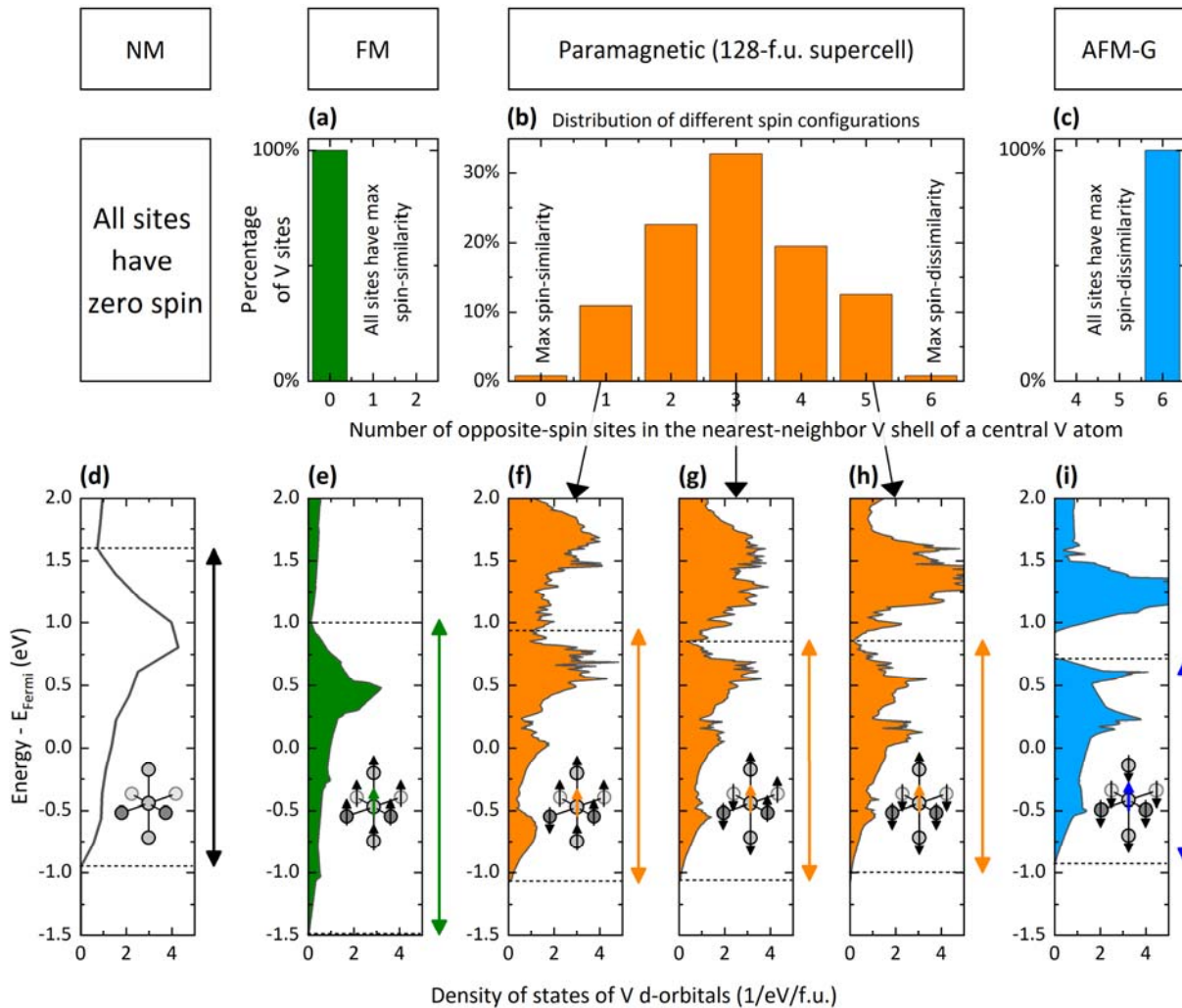


Figure 4 (2 columns) | Total DOS of cubic SrVO₃ (the same PBE+U method) as a weighted superposition of the partial DOS (PDOS) of the local spin motifs. Upper panel -- the weight of local spin configuration in: (a) Statistical weights of FM primitive cell (all the first-neighbor vanadium have the *same* spin direction as the center vanadium, see insert in (a)); (b) distribution of statistical weights of different spin configurations in the cubic PM supercell; (c) statistical weights of AFM-G double perovskite cell (all the first neighbor vanadium have the *opposite* spin direction to the center vanadium, see insert in (c)). Lower panel -- the vanadium *d*-PDOS in different spin configurations: (d) NM primitive cell in which each all site has zero spin; (e) FM motif; (f)-(h) different local spin motifs in PM phase, and (i) AFM-G motif. The dash lines and vertical arrows in (d)-(i) show the bandwidths of *d*-orbital for guide of eyes. Note that in (d)-(i) we only show the *d*-PDOS of the central vanadium atoms (neighbors are not included to avoid multiple counting).

IV. Positional symmetry breaking causes coupling of the electronic bands leading to mass enhancement.

A. Octahedral rotation enhances masses in *s-p* halide perovskite CsPbI₃

Octahedral tilting (rotations) [43] have been known for long to exist in perovskites; here, we point out that such observed local modes can cause mass enhancement. The perovskite structure consists of corner-sharing octahedra, that allow octahedral rotation and tilting. The classic atomic size mismatch between the A and B sublattices in ABX₃ drives static octahedral tilting and rotations, as was recognized already in 1926 [87] and verified by modern PDF measurements [88] as well as by DFT total energy minimization [52,89–92]. This kind of deformation derives from classical atomic size mismatch and therefore exists even in close-shell *s-p* electron compounds such as halide perovskites [52,90,91]. Octahedral tilting (rotation) effects have been investigated in lead and tin halide perovskites for the low temperature *tetragonal and orthorhombic phases*. However, for the *cubic phase*, it has been generally assumed [30–33] that because of its XRD designation as the $Pm\bar{3}m$ structure with a single formula unit per cell, such tilting is disallowed by symmetry hence absent. Here we point out that (i) a minimal 2×2×2 cubic supercell is needed to reveal tilting, (ii) *single* tilting modes [43] already change the mass, and (iii) larger supercells such as 4×4×4 can reveal *multi-mode* tilting, showing further lowering of the total energy relative to the monomorphous $Pm\bar{3}m$ cubic model. Such multi modes significantly affect mass enhancement. Although technically this can be posed as an electron-phonon effect, given that the pattern of tilting and atomic displacements are complex and imply the participation of a significant number of phonons, we do not use the phonon terminology; instead, we explicitly (and non-perturbatively) minimize the generally anharmonic DFT energy surface with respect to all atomic positions, dislodge atoms from metastable local positions to stable positions, then calculate the ensuing band structure and masses.

Qualitative analysis of how octahedral tilting affects band edge energies in CsPbI₃. The coupling between octahedral tilting and electronic structure in low-temperature phases has been discussed in oxide [5] and halide perovskites [30] as a band-gap-tuning mechanism. Here as schematically shown in [Figure 5](#), we demonstrate how the octahedral rotation in *s-p* bonded compound CsPbI₃ affects band edge states. In cubic CsPbI₃ without distortion, the valence band maximum (VBM) is an antibonding state formed from the Pb-*s* and I-*p* orbitals, while the conduction band minimum (CBM) is weakly antibonding state of Pb-*p* and I-*p* orbitals. Allowing rotations of the (PbI₆) octahedron will weaken both the *p-p* and *s-p* bonding between Pb and I. Consequently, being antibonding states, *both CBM and VBM* will move to *lower* energies. However, because the VBM is more

sensitive to octahedral deformation (being composed of inner-shell $6s-3p$ antibonding) than the CBM (being composed of outer shell $6p-3p$ antibonding) [93], the VBM will move further than CBM, leading to a larger band gap due to rotation (Figure 5, right panel).

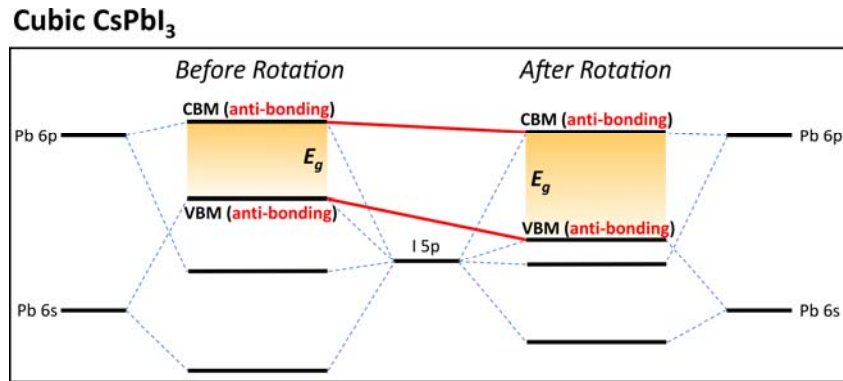


Figure 5 (1.5 columns) | Energy level diagram for CsPbI_3 , before and after octahedral rotation. The red solid lines show the trends of band gap change.

Model DFT calculations on the effect of frozen rotations on mass enhancement in CsPbI_3 . The results of the simple model of Figure 5 are then validated by DFT calculations of small (8-f.u.) model supercells where we artificially impose given octahedral rotation angles, followed by band unfolding to the single-cell cubic primitive Brillouin zone. The unfolded band structure is shown in Figure 6. The imposed octahedral rotation here is $a^+a^-a^-$ mode (Glazer notation [43]) or T_2 (irreducible representation from S. C. Miller and W. F. Love [94]). It can be seen that the imposed octahedral rotations can affect the curvature of both valence and conduction bands at the band edges. Choosing the band gap and effective masses of the zero-rotated structures as the reference, as shown in Figure 6, one can see that under an uniformed arbitrary rotation of $(10^\circ, 10^\circ, 10^\circ)$, the band gap of CsPbI_3 increases by 0.52 eV ($\sim 40\%$), and the electron and hole masses are enhanced by 77% and 113%, respectively.

CsPbI₃ (nonmagnetic cubic phase + artificial tilting, PBE)

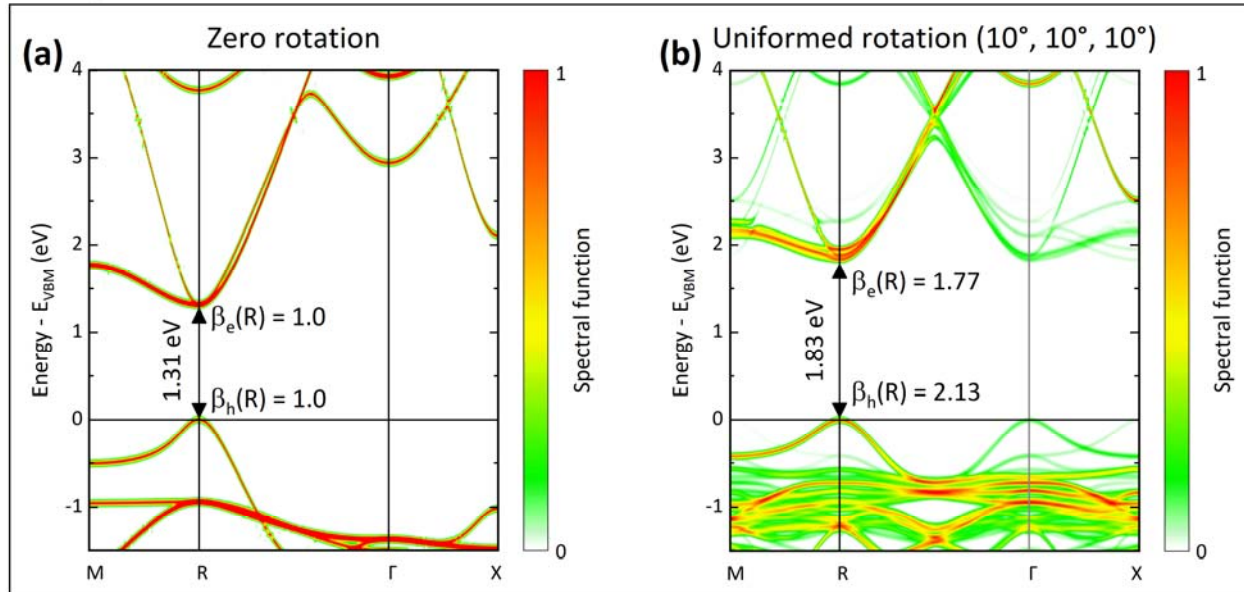


Figure 6 (2 columns) | The unfolded spectral function (EBS) in the cubic primitive Brillouin zone, before (a) and after (b) a uniformed (10°, 10°, 10°) $a^+a^-a^-$ rotation for cubic CsPbI₃. Both (a) and (b) are calculated using the 8-f.u. supercell. Note that EBS shown in (a) is identical to the band structure obtained from a minimal-cell cubic model because (a) has no atomic distortion. Band gap is 1.31 eV in (a) and 1.83 eV in (b). Taking effective masses of CBM and VBM in (a) as references, the mass enhancement factors in (b) are $\beta_e=1.77$ (for electron, counting all 3 states near CBM) and $\beta_h=2.13$ (for hole), respectively. All masses come from band dispersion (second derivative of E vs k).

Full supercell calculation of rotation-induced mass enhancement in CsPbI₃. Having clarified the effect of classical rotation on the band structure by the model (Figure 5) and validated it by DFT (Figure 6), we next study a large supercell with optimized rotating geometries in the cubic phase of CsPbI₃. Recall that the rotations discussed here are not thermal, but, in fact, they are energy-lowering distortions derived by the nature of the chemical bonds (here, steric effects) even at low temperatures. Thus, we obtain these deformations by minimization of the DFT internal energy. But this requires that we allow a larger than the minimal unit cell so that rotations can be accommodated geometrically. The electronic structure of a single-cell cubic ($Pm\bar{3}m$) model (monomorphous models) is shown in Figure 7(a). Restricted by the small size and periodic boundary condition, such structure cannot accommodate rotations (as shown by the blue lines in Figure 7(b)). We avoid such restrictive assumption using a supercell representation (32-f.u. supercell) instead. We perform a *constrained minimization* of the internal energy (T=0) of the cubic phase that retains the macroscopic cubic

supercell shape (or else the minimization will converge to the ground-state orthorhombic or tetragonal structures that are not the subject of the current study). At the same time, we allow all cell-internal degrees of freedom to locally adjust to find the structure with the lowest total energy. This is done by using a set of random initial nudging, so as to dislocate atoms from possible local minima.

It has been shown in our recent study [36] that for lead halide perovskites with organic molecules on the A-site, such supercell representation following the constrained DFT total-energy minimization explains various anomalies in the cubic phase, where the minimal-cell model disagrees with experimental observation. This includes a close agreement with the measured pair distribution function, significant increase in the band gap, and dielectric constant. For the cubic CsPbI₃ supercell, we have found that when abandoning the restriction of the minimal-cell model, the atomic configuration of cubic phase that gives the lowest total energy of the cubic phase (the supercell out-shape has been constrained to be cubic), is not the single-f.u. $Pm\bar{3}m$ cubic model, but a supercell representation for the cubic phase with many local octahedral tilting. The many local tilting in the cubic supercell cannot be written using the simple Glazer notations but must involving the complex notations [43], and cannot be reduced into smaller cell models. We find that: (i) the rotation angles are distributed among 5-13° (red lines in Figure 7(b)(e)); (ii) the supercells have lower total energy (-124.4 meV/f.u.) compared with the single-cell model. Recall that during the DFT calculation, we used the equivalent k-point mesh for all cells (12×12×12 Γ -center k-point mesh in primitive cubic BZ) and a total-energy tolerance of 10⁻⁸ eV/atom, we, therefore, suggest that the -124.4 meV/f.u. energy lowering is robust. Furthermore, (iii) we find, as expected from the simple model of Figure 5, a significant band gap increase and thus mass enhancement factors: the band gap increases from 1.31 eV in the monomorphous single-cell model to 1.85 eV in the polymorphous supercell model (the measured band gap is E_g=1.73 eV [30]) leading to mass enhancements $\beta_e=1.8$ and $\beta_h=2.2$ for electrons and holes, respectively (Figure 7(a)(c)). Although, as far as we know, the effective mass has not been reported from experiments for cubic CsPbI₃, the reduced mass ($m^* = -m_e^*m_h^*/(m_e^* + m_h^*)$) for cubic CsPbBr₂ has been measured [70] as $m^*=0.12\pm 0.01 m_0$, which is close to our prediction (masses are calculated via the second derivative of E vs k) here $m^*=0.14m_0$ using symmetry-broken DFT. Recall that neglecting the distortions gives a mass 1.8 times smaller. We conclude that semiclassical octahedral rotations in ABX₃ can derive quantum mechanical band gap increases and significant mass enhancements. The same physics is expected to contribute to oxides; the magnitude of the effect would naturally depend on the extent of rotations and the response of the host crystal to deformations.

CsPbI₃ (nonmagnetic cubic phase, PBE)

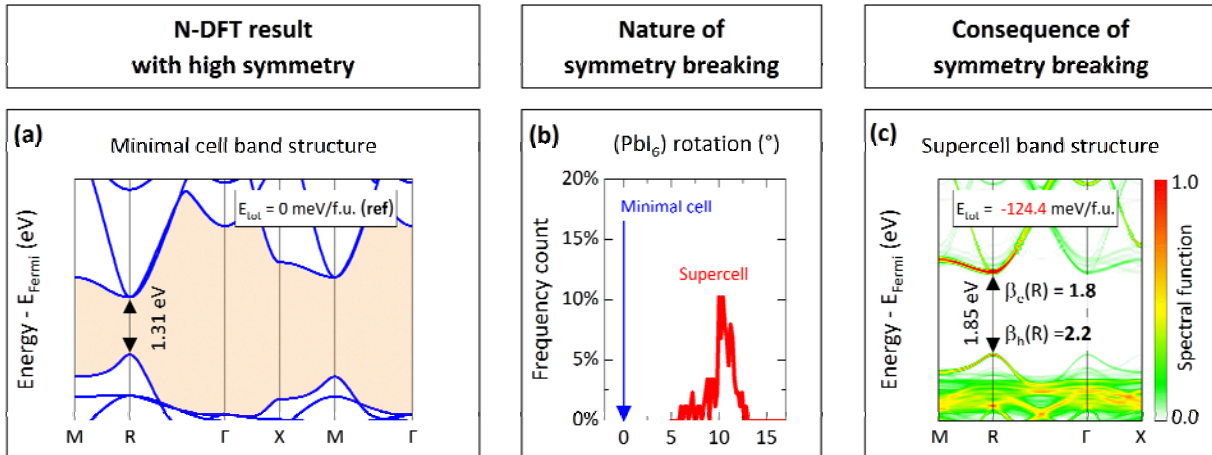


Figure 7 (2 columns) | Mass enhancements in cubic CsPbI₃. (a) The band structure from the same N-DFT restriction as in previous literature [30–33], namely a single-cell cubic model, using PBE functional. (b) gives the distribution of octahedral rotation angles. The blue arrow in (b) shows that in the minimal cell model all octahedra have zero rotation, while the red curve shows that in supercell different octahedra have a distribution of different, non-zero rotations. (c) shows the unfolded band structure when removing the minimal-cell restrictions by using instead a cubic, 32-f.u. supercell CsPbI₃ with the same PBE method. Masses in (c) are calculated via the second derivative of E vs k , which gives $\beta_c = 1.8$ and $\beta_h = 2.2$. To the best of our knowledge, the experimental measurement for separate electron and hole masses for cubic CsPbI₃ has not been reported yet; while for cubic CsPbBr₃ the reduced mass m^* has been reported as $0.12m_0$, very similar to the reduced mass calculated from (c) which is $0.14m_0$, but 1.8 times heavier than the reduced mass from (a) which is $0.07m_0$.

B. Jahn-Teller-like distortion enhances masses in LaMnO₃

To draw the analogy between mass enhancement in s - p bonding perovskites (previous section) and the better-known effect in d -electron perovskites, we treat next the compound LaMnO₃. The observed positional symmetry breaking in orthorhombic LaMnO₃ is a pseudo-Jahn-Teller distortion, leading to inequivalent Mn-O bond lengths in MnO₆ octahedron. It has been previously argued that such Jahn-Teller distortion is specifically attributed to dynamic correlations [53], and that mean-field DFT fails to predict the ensuing structural or electronic properties [95]. Previous DFT+U calculations reproducing the Jahn-Teller distortion in the orthorhombic LaMnO₃ [96–98] gave perhaps the impression that the presence of +U in DFT implies the same correlation role as +U in the Hubbard Hamiltonian. More recently, Varignon et al. [99] showed that DFT without U is already enough to capture such distortions, provided that a more accurate exchange-correlation functional

was used. It was also clarified [100] that proper Jahn-Teller distortion is associated with degeneracy removal (*i.e.*, electronic instability such as the Q_2^- mode [101]), whereas the Q_2^+ mode [101] originates from classic steric effects (the Goldschmidt tolerance) that can be classified as *pseudo*-Jahn-Teller distortions. Here, we show that such modes cause mass enhancement.

Figure 8(c)(d) show the atomic structure and band structure of orthorhombic AFM cell with Q_2^+ deformation taken from previous DFT calculation [100]; while Figure 8(a)(b) show the atomic structure and band structure of the same AFM cell (the same AFM order, the same octahedral rotation and octahedral volume) as (a)(b) but only removing the Q_2^+ deformation. Such Q_2^+ -free model (Figure 8(a)(b)) has been used as the DFT model in previous studies, giving metallic behavior [53,102,103]. Both cases are calculated using SCAN functional. The band structure lacking the Q_2^+ mode (b) is metallic, while the band structure with Q_2^+ mode (d) is gapped. Using (b) as the reference and considering the bandwidths of Mn- d e_g bands in (d), the bandwidth enhancement factors is $\beta_e=1.8\pm 0.5$ and $\beta_h=1.6\pm 0.4$, for electrons and holes, respectively; the uncertainty is due to that bandwidths along different k paths give different enhancement factors. The enhancement factor obtained by DMFT with Q_2^+ deformation is $\beta_h=1.3-1.7$ (values are extracted by comparing this work with results reported in DMFT reference [53]), and comparable to experimental observation of $\beta_h=2.6-2.8$ in $\text{La}_{0.6}\text{Sr}_{0.4}\text{MnO}_3$ [72]. We conclude that pseudo-Jahn-Teller distortion Q_2^+ captured by mean-field DFT is capable of producing significant mass renormalizations, even though on this case both DFT and DMFT give smaller renormalization than what was measured, which may be due to the A-site alloy effect in the measured sample $\text{La}_{0.6}\text{Sr}_{0.4}\text{MnO}_3$ [72].

LaMnO₃ (orthorhombic AFM phase, SCAN)

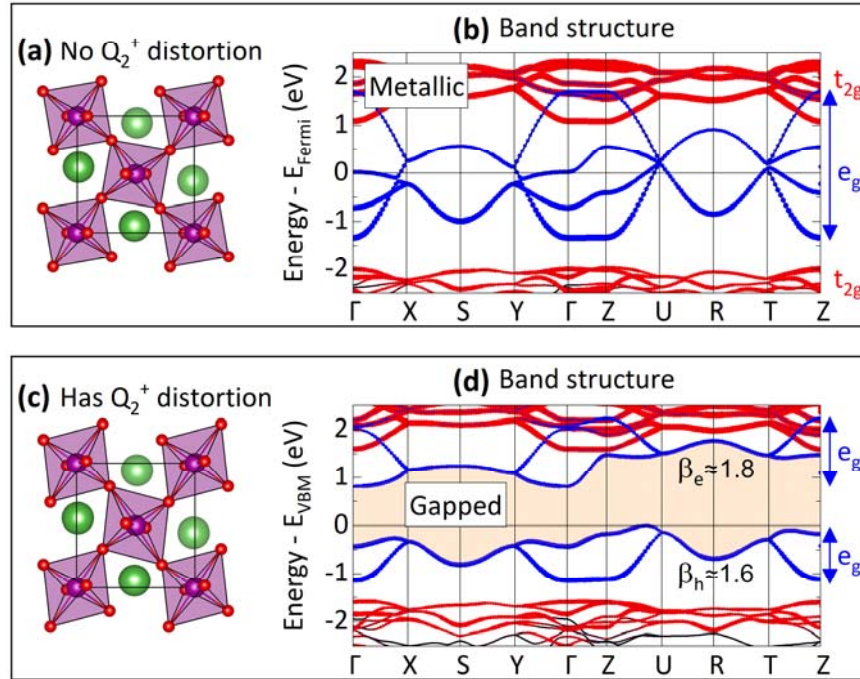


Figure 8 (1.5 columns) | Mass enhancements in AFM orthorhombic phase of LaMnO₃. (a) shows the atomic structure and (b) gives the band structure with no Jahn-Teller-like Q_2^+ distortion, using SCAN functional. The system is metallic and has a broad Mn e_g band (bandwidth is denoted by the blue arrow on the right side of (b)) crossing the Fermi level. (c) shows the atomic structure and the (d) gives the band structure when considering the correct Q_2^+ distortion with the same SCAN functional, where the gap opens between the two Mn e_g bands (bandwidths are denoted by blue arrows on the right side of (d)). Red and blue circle symbols in (b) and (d) denote the orbital projections of Mn- d t_{2g} and e_g orbitals, respectively; other orbitals are not shown here; the size of the circle is proportional to the composition of orbital. Mass enhancements in (d) with respect to (b) are calculated via the bandwidths of Mn e_g bands, which give $\beta_e \approx 1.8 \pm 0.5$ and $\beta_h \approx 1.6 \pm 0.4$ (uncertainty is due to that bandwidths along different k paths give different enhancement factors).

C. Bond disproportionation enhances masses in SrBiO₃

Bond disproportionation in perovskites corresponds to the spontaneous transformation of two equal octahedra into two inequivalent octahedra, also known as octahedral breathing distortion, belonging to M_1^+ or R_1^+ mode [104]. A cell model of ABX₃ containing a single formula unit allows obviously but a single volume for all (BX₆) octahedra, while some compounds, *e.g.*, SrBiO₃ and BaBiO₃ [29] prefer bond disproportionation on B ions, appearing as some octahedra dilate while others contract, eventually leading to multiple local environments

instead of a single local environment. Total energy calculations [105] show that this disproportionation is energy lowering, not a transition between two phases.

We choose SrBiO₃ as an example to investigate such bond disproportionation effect on effective masses. SrBiO₃ is known to be insulating in its low-temperature monoclinic phase with a disproportionate R_1^+ distortion [106]. The monoclinic phase shows tilting $M_3^+ \oplus R_4^+$ mode (Glazer notation $a^+b^-c^-$), which could also contribute to the mass enhancement. To isolate the contribution of R_1^+ disproportionation from tilting, we apply here a three-level model: (1) We start from level-1 model, which is minimal-cell cubic, $Pm\bar{3}m$ structure, then we (2) apply *tilting* $M_3^+ \oplus R_4^+$ mode to construct level-2 a monoclinic ($P2_1/n$) structure without disproportionation, and finally (3) level-3 model uses the experimentally observed SrBiO₃ monoclinic phase (also $P2_1/n$) with both tilting (the same amplitude as in level-2) and disproportionation. The atomic structures, together with the band structures using the PBE functional + SOC effect for such three levels, are shown in [Figure 9](#).

(1) Level-1 ($Pm\bar{3}m$ cubic; [Figure 9\(a,b\)](#)) is a p-type degenerate metal, as its Fermi level crosses its wide (as denoted by the blue arrow on the right side of [Figure 9\(b\)](#)), principal valence band made of O- p orbitals. The total DFT energy of level-1 is extremely high (+980 meV/f.u. above the convex hull), clarifying that it is not a low-temperature ground state. (2) Level-2 monoclinic phase without disproportionating R_1^+ distortion ([Figure 9\(c,d\)](#)) shows a more compact O- p valence band, however, it is still a p-type gapped metal, *i.e.*, the octahedral tilting cannot open the gap. The total DFT energy of level-2 is 71 meV/f.u. above the convex hull. Finally, (3) level-3 the monoclinic phase with disproportionate R_1^+ distortion (experimental structure; [Figure 9\(e,f\)](#)) shows semiconducting behavior with a 0.26 eV gap between the two split O- p bands, a splitting induced by the bond disproportionation. Level-3 is at on the convex hull (*i.e.*, the ground state). Nevertheless, as seen in [Figure 9](#), the disproportionating R_1^+ distortion is the key to band gap opening, therefore, the most interesting mass enhancement is the one from level-2 to level-3 $\beta(L3:L2)$. Considering the bandwidths of O- p bands in [Figure 9\(d\)](#) and (f), if using [Figure 9\(d\)](#) as the reference, the bandwidth-related masses in [Figure 9\(f\)](#) have the enhancement factors of $\beta_e(L3:L2)=1.3\pm0.2$ and $\beta_h(L3:L2)=1.5\pm0.2$; the uncertainty is due to that bandwidths along different k paths give different enhancement factors. We conclude that disproportionation symmetry breaking, an effect that exists both in s - p perovskites as well as in d -electron perovskites, is capable of significant mass enhancement.

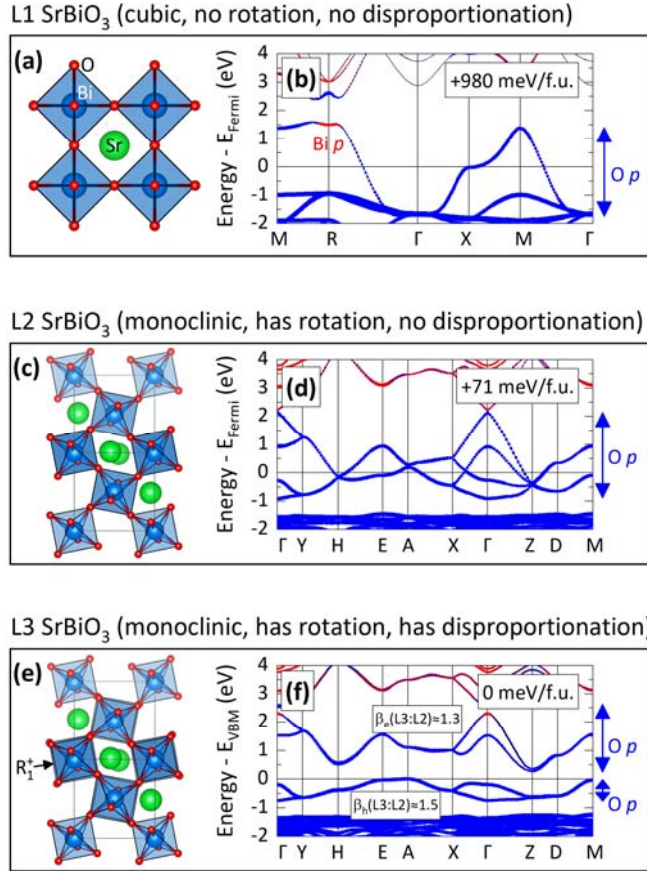


Figure 9 (1 column) | Mass enhancements in SrBiO₃. (a) shows the atomic structure and (b) gives the band structure from the $Pm\bar{3}m$ phase, using PBE functional (level-1, L1). The system is metallic and has a broad O- p band (blue arrow on the right side of (b)). (c) shows the atomic structure and the (d) gives the band structure when allowing the observed (monoclinic) octahedral rotations, but no disproportionate R_1^+ distortion, with the same PBE functional (level-2, L2), where the O- p bands become more compact, but the system stays metallic. (e) shows the atomic structure and the (f) gives the band structure when allowing all experimentally observed distortions, with the same PBE functional (level-3, L3), which leads to the O- p bands splitting and hence a band gap opening. The R_1^+ distortion can be seen by the slightly different octahedral volumes in (e) (black arrow). Red and blue circle symbols in (b) (d) and (f) denote the orbital projections of Bi- p and O- p orbitals, respectively; other orbitals are not shown here; the size of the circle is proportional to the composition of orbital. Mass enhancements in (f) with respect to (d), *i.e.*, $\beta(L3:L2)$, are calculated via the bandwidths of O- p bands, which give $\beta_e=1.3\pm 0.2$ and $\beta_h=1.5\pm 0.2$; the uncertainty is due to that bandwidths along different k paths give different enhancement factors. The same PBE method with spin-orbit coupling has been applied for all SrBiO₃ calculations.

V. Not all positional symmetry breakings lead to significant mass enhancement.

The examples shown in section IV A, B, and C indicate cases where symmetry breakings result in large energy-lowering and they couple significantly to the electronic manifold, altering its band structure, including effective mass enhancement. There are, however, cases where such deformations are small, or even if not small, they might couple only weakly to the electronic states that form the band edges, *i.e.*, small deformation potentials, leading to small or negligible mass enhancement. We next illustrate two such examples.

A. Weak octahedral rotations in intrinsic SrTiO₃ cause negligible mass enhancement.

Undoped SrTiO₃ is a nonmagnetic insulator. Positional distortions, such as the octahedral tilting in SrTiO₃ (also known as the antiferrodistortive displacement, AFD), have been noted in the low-symmetry tetragonal phase [107–109], but *absent* in the cubic phase [109–112]. Some observations of distortion in the cubic phase were then attributed to extrinsic factors such as strain [113–116], defects [117], impurities [118], interface [119], or thermal effect [120]. Indeed, AFD is not expected theoretically in the cubic phase unless one abandons the conventional single formula unit monomorphous description of the $Pm\bar{3}m$ XRD model and allows tilting degree of freedom in a supercell description of the cubic phase. As Table I indicates, here, we focus on the properties of the cubic phase, not the low-temperature ground state, performing a minimization of the cubically constrained total energy as a function of the cell internal atomic positions.

When doped n-type, *e.g.*, SrTiO₃:Nb or SrTiO₃:La at doping concentration of 0.01-0.05 electron/f.u., one observes (i) the formation of a low dispersion (heavy mass) occupied *in-gap* states [121–123], as well as (ii) a Fermi level inside the broad (light mass) principal conduction band. Using plasma frequency as a measure for electron mass $\omega^2 = n_c/m^*$, where n_c is the free carrier concentration, large values of electron mass enhancement of $\beta_e=2-3$ [73] were reported. We find that even if removing the single-cell restrictions used in previous studies (*i.e.*, $Pm\bar{3}m$ minimal cell with a single f.u., as shown in Figure 10(a)) by constructing a supercell (here, 64-f.u.) and relaxing all internal atomic positions, the cubic phase SrTiO₃ shows only small octahedral rotations around 3-4 degrees (shown in Figure 10(b)), a small total energy lowering of -4.4 meV/f.u., and negligible enhancements for both electron and hole masses (Figure 10(c); $\beta_e \approx 1.1$ and $\beta_h \approx 1.1$, both calculated from the second derivative of E vs k). Thus, our calculated value pertaining to the principle conduction band (not in-gap polaron like state) $\beta_e \approx 1.1$ indicates negligible enhancement. In the doping concentration 0.05 electron/f.u., both DMFT [110] and N-DFT [110] calculations predict similar electron mass, indicating no mass enhancement by strong electron correlations. It is not clear if the observed substantial electron mass enhancement is related to the presence of polaron states [(i) above] or is intrinsic [(ii) above, due to electron

doping [117,118,124] of main conduction band]. Indeed, the plasma frequency mass enhancement $\beta = \omega_{\text{model}}^2/\omega_{\text{exp}}^2$ may be affected by doping compensation, reducing the effective concentration of free carriers. The experimental values of mass enhancement in SrTiO₃ appear to require clarification.

SrTiO₃ (nonmagnetic cubic phase, undoped, SCAN)

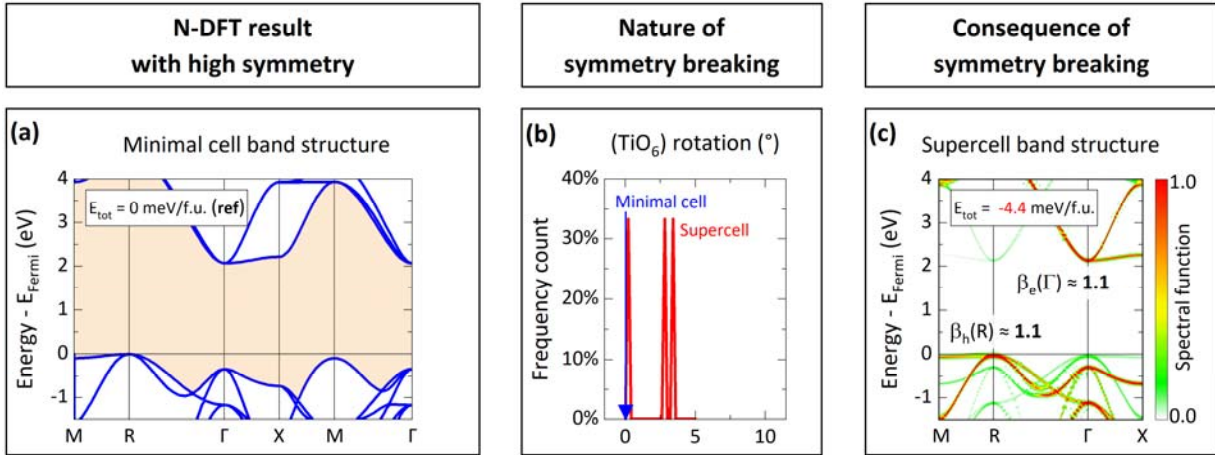


Figure 10 (2 columns) | Mass enhancement in the nonmagnetic cubic phase of SrTiO₃. (a) shows the band structure (from the same N-DFT restriction as in previous literature [110–112], namely a single-cell, cubic, NM SrTiO₃ model, using SCAN functional. (b) shows the distribution of octahedral rotation angles. The blue arrow in (b) shows that in the minimal cell model all octahedra have zero rotation, while the red curve shows that in supercell different octahedra have a distribution of tiny rotations around 3-4 degrees. (c) shows the unfolded band structure when removing the minimal-cell restrictions by using instead a cubic, 64-fu NM supercell SrTiO₃ with the same SCAN method. Masses in (c) are calculated via the second derivative of E vs k , which gives $\beta_e \approx 1.1$ and $\beta_h \approx 1.1$.

B. Antiferroelectric and paraelectric displacements in BaTiO₃ have negligible effects on masses

Another well-known case where local atomic displacement occur involves ferroelectric (FE) compounds, often having paraelectric (PE) and antiferroelectric (AFE) phases. BaTiO₃ is one of the first-found FE perovskite compounds [125–127], where the ferroelectricity is induced by the off-center displacement of the Ti atom in (TiO₆) octahedron. BaTiO₃ experiences a complex phase transition, from rhombohedral (R, <180 K) to orthorhombic (O, <280 K), to tetragonal (T, <400 K), to cubic (C) [128]. While its R, O, and T phases all show ferroelectricity, the high-T cubic phase shows no net ferroelectricity. Therefore, it has been argued that such cubic phase has no Ti atom off-center displacement in any octahedra (*i.e.*, a non-electric (NE) phase) and can be represented by a minimal cubic cell model [129–131]. However, recent investigations show that such

minimal-cell, NE cubic model cannot explain the Raman and X-ray fine structure (XAFS) observations, and the cubic phase could be instead an AFE phase [44] or a PE phase [132]. Here we aim to study if the AFE and PE nature in cubic BaTiO₃ can have effects on its electronic properties, such as band gap and effective mass.

The AFE phase is mimicked by an 8-f.u. supercell, constraining its lattice vectors to the macroscopically observed cubic structure while relaxing all cell-internal atoms. Figure 11(a) shows the band structure of the non-electric model (single-f.u., NE cubic model) using the SCAN functional. The difference between the atomic positions in the NE monomorphous model and the AFE polymorphous supercell is plotted in Figure 11(b): The monomorphous cell has no Ti-atom displacement ($\Delta R_i=0$ for every Ti), while the AFE supercell shows a unique displacement pattern, where the eight Ti atoms move along the eight $\langle 111 \rangle$ directions (*i.e.*, [111], [11-1], [1-1-1], ...); although the AFE supercell has a zero net polarization ($\langle \Delta \mathbf{R} \rangle = 0$), the local polarization on each Ti site is non-zero and as large as 0.13 Å ($\langle |\Delta \mathbf{R}| \rangle = 0.13$ Å). Other distortions (rotations, Jahn-Teller distortion, *etc.*) have all been found to be negligible in the AFE supercell. This AFE displacement pattern agrees well with the previous theory [44]. Figure 11(c) shows the unfolded band structure of the AFE supercell. We found that although the AFE displacement is large, the mass enhancement is still negligible ($\beta_e \approx 1.1$ and $\beta_h \approx 1$), in other words, the electronic response to such displacements (deformation potential) must be small.

This weak response of band-edge states to Ti off-center displacement can be understood by considering the symmetry mismatch between the orbitals making up the VBM and CBM, and the symmetry of the Ti displacement mode: In the cubic primitive-cell of BaTiO₃ (non-electric single-f.u. model without displacements or tilting), the system has the space group of $Pm\bar{3}m$, where, according to the molecular orbital theory for octahedral O_h symmetry [133], the CBM is pure Ti-*d* orbital (irreducible representation T_{2g}), and the VBM is made up by O-2*p* + Ti-4*p* orbitals (irreducible representation T_{1u}). Considering that the Ti-4*p* orbital is very high in energy, the VBM is almost pure O-*p* (T_{1u}). On the other hand, our supercell model of the AFE state has a large M_2^- distortion mode due to *Ti displacements* (amplitude = 0.15 Å, irreducible representation B_{1u} for D_{4h} symmetry) whereas *tilting and rotation* amplitudes are all smaller than 6×10^{-4} Å. Since the VBM and CBM are not B_{1u} symmetric, they do not respond to the Ti displacements, thus the AFE supercell only shows negligible mass enhancement for these states.

BaTiO₃ (anti-ferroelectric cubic phase, SCAN)

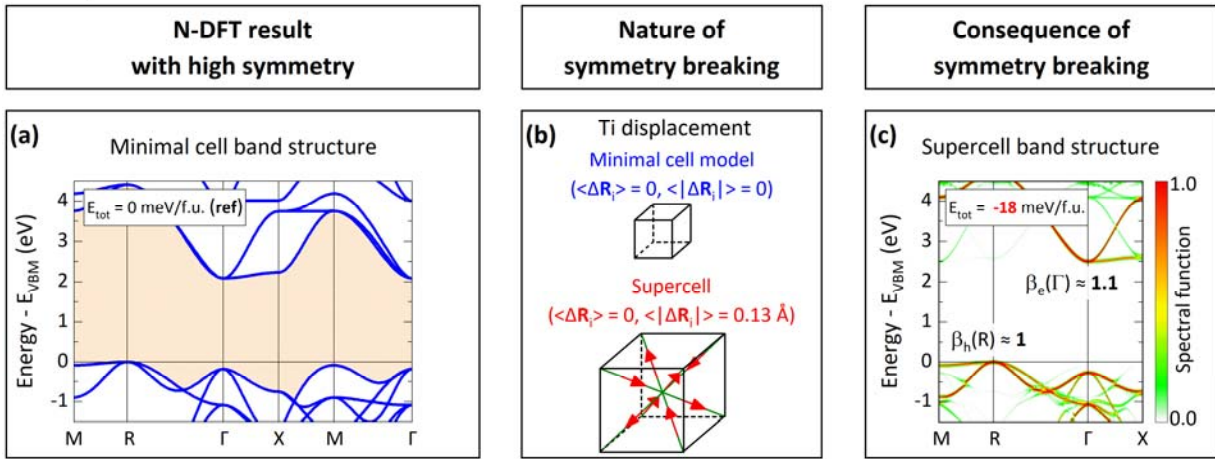


Figure 11 (2 columns) | Mass enhancements in AFE cubic phase of BaTiO₃. (a) shows the band structure from the same N-DFT restriction as in previous literature [129–131], namely a single-cell, no Ti-atom displacement model, using SCAN functional. (b) gives the distribution of Ti-atom displacements symmetry breaking: Upper part in (b) shows that the minimal-cell model BaTiO₃ does not have any Ti-atom displacement ($\Delta \mathbf{R}=0$ for each Ti atom), while the lower part in (b) shows that the AFE supercell (8 f.u.) has a unique displacement pattern, where the 8 Ti atoms move along 8 $\langle 111 \rangle$ directions. In the AFE supercell, the net polarization is zero ($\langle \Delta \mathbf{R} \rangle = 0$), but the local polarization on each Ti site is large ($\langle |\Delta \mathbf{R}| \rangle \approx 0.13 \text{ \AA}$). (c) shows the unfolded band structure of the 8-f.u. AFE supercell BaTiO₃ with the same SCAN method. Masses in (c) are calculated via the second derivative of E vs k , which gives $\beta_e \approx 1.1$ and $\beta_h \approx 1$.

The PE phase has been modeled by a 32-f.u. supercell. After the atomic relaxation, all Ti atoms have developed non-zero, non-uniformed local polarizations, as shown by the red curved in Figure 12(b). It can be seen that the Ti displacement forms a distribution not only on amplitude but also on directions. We note that the net displacement (vector summation of all Ti displacements) is not zero (0.1 Å per f.u.), because we do not force any net-polarization condition during the supercell relaxation, and the supercell is, in fact, weak FE. Nevertheless, the nature of a distribution of static (non-thermal), different displacement in the supercell is by itself different than the low-T FE phase. Solving the band structure and doing band unfolding (Figure 12(c)) shows small mass enhancement of $\beta_e \approx 1.1$ and $\beta_h \approx 1$. The results of both AFE and PE seem consistent in that the coupling of polarization to VBM and CBM states is weak, illustrating cases that the ferroelectric displacement has a negligible effect on mass enhancement.

BaTiO₃ (paraelectric cubic phase, SCAN)

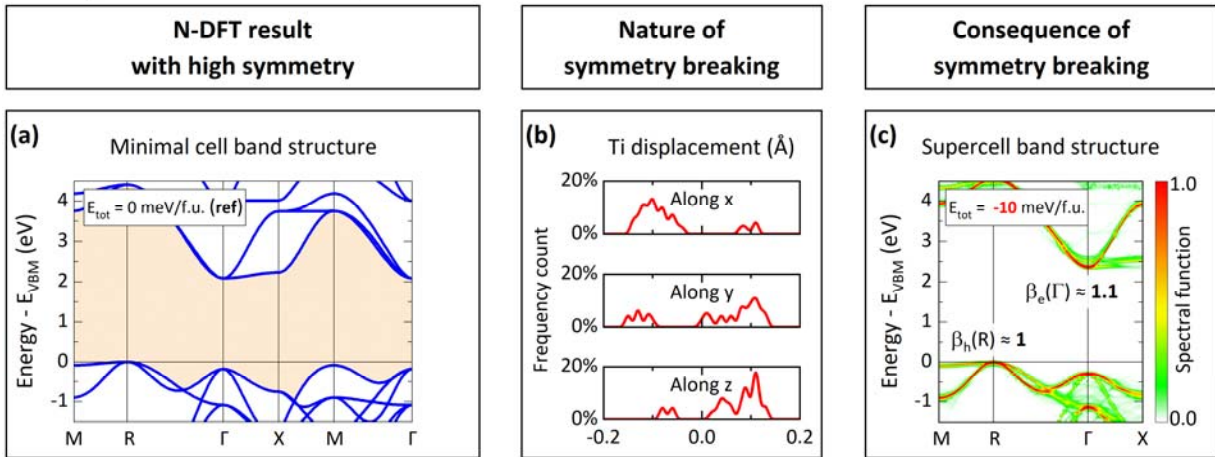


Figure 12 (2 columns) | Mass enhancements in the PE cubic phase of BaTiO₃. (a) shows the band structure from the same N-DFT restriction as in previous literature [129–131], identical to Figure 11(a). (b) gives the distribution of Ti-atom displacements in the 32-f.u. PE supercell after atomic relaxation along x, y, and z directions ([100], [010], and [001] directions). (c) shows the unfolded band structure of the 32-f.u. PE supercell BaTiO₃ with the same SCAN method. Masses in (c) are calculated via the second derivative of E vs k , which gives $\beta_e \approx 1.1$ and $\beta_h \approx 1$.

VI. Conclusions

Symmetry-breaking DFT captures many of the mass enhancement effects previously attributed exclusively to strong electronic correlations under restricted symmetry. Whereas the theoretical methodology of supercell DFT has surely been used in previous studies on many different effects [26], the insights that mass enhancement can be described by mean-field DFT with broken symmetries rather than exclusively by symmetry-restricted many-body approach is noteworthy. The current study further provides a general and intuitive explanation for the physical origins of mass enhancement, as summarized in Fig. 1, including spin symmetry-broken and positional symmetry-broken effects. There are cases where the coupling of distortions to the electronic states at band edges are weak, causing negligible mass renormalization (*e.g.*, SrTiO₃ where the distortion is small, or BaTiO₃ where only Ti displacement not tilting lowers the total energy), yet other cases where the distortions and their coupling are strong, leading to large enhancement factors (*e.g.*, SrVO₃, CsPbI₃, LaMnO₃, and SrBiO₃), even by the single-determinant mean-field DFT method, which sometimes are even comparable to the mass enhancement suggested by the high-order dynamical electron-electron correlation theory. The presence of

mass enhancement in the considered systems is not necessarily evidence for the exclusive need for strong dynamically correlated methodologies [15–24].

For the PM phase, in a *symmetry-restricted* many-body approach (a) containing a single magnetic moment (monomorphous limit) interacting with an average bath, the magnetic moment must fluctuate in time to conserve the zero total moment expected of a paramagnet. In principle, the spin fluctuations in a non-vibrating lattice can be either (i) longitudinal (single-site spin flip or inter-site spin hopping) or (ii) transversal (single-site spin rotation or spin-wave excitation). The longitudinal fluctuations can be rather fast, e.g., a few femtoseconds, in a metallic system, but slow and very rare in insulators due to the large energy cost of overcoming the band gap. The transversal fluctuations, on the other hand, are typically much slower but not significantly dependent on the metallicity, e.g., in the ordered magnetic ground state of Fe, Ni, and Co, the spin-wave excitations evolve within 1 ps [134], while in the PM state of small-gap semiconductor CrN, individual moments rotate with respect to its neighbors in the time scale of 50-100 fs [135]. Since ARPES measurement can be done in a time scale of femtosecond [136], spin fluctuation effects longer than this time scale (longitudinal ones in insulators, and transversal ones in both insulators and metals) will be measured as the time average over many properties of individual spin configurations (average of the properties), while spin fluctuation effects shorter than a few femtoseconds (longitudinal ones in some metals) will be observed as the properties of a time-averaged spin configuration (property of the average).

In a *symmetry-broken* representation (b) containing a polymorphous distribution of many local moments, as used in the present paper, the orientation of the moment is static, but there are many orientations resolved spatially. In both cases (a) and (b) the average moment is zero (time average in symmetry-restricted approach and spatial average in symmetry-broken approach) as required of the PM state, while by ergodicity the symmetry-broken approach with static, spatial distribution of individual moments is able to reproduce the ARPES observation if the spin fluctuations are longer than a few femtoseconds (e.g., longitudinal ones in insulators, and transversal ones in both insulators and metals).

Acknowledgement

The work at the University of Colorado at Boulder was supported by the U.S. Department of Energy, Office of Science, Basic Energy Sciences, Materials Sciences and Engineering Division, under Grant No. DE-SC0010467 to the University of Colorado. The *ab initio* calculations in this work were performed using resources of the

National Energy Research Scientific Computing Center, which is supported by the Office of Science of the U.S. Department of Energy.

Appendix A: DFT details.

To calculate the total energy, band structure, and effective mass, the plane wave pseudopotential DFT method, as implemented in the VASP software package [137,138] has been used. (i) For transition metal oxides with localized orbitals SrTiO₃, BaTiO₃, and LaMnO₃, the SCAN functional [139], used previously [99,140] has been applied. (ii) For metallic SrVO₃, such SCAN functional could not reach a self-converged charge density in our large PM cubic supercell (640 atom/f.u.); therefore, for all SrVO₃ cells, the Perdew–Burke–Ernzerhof (PBE) functional + U (with $U=1.25$ eV on V-d orbitals) used previously [27] has been applied instead. Figure 13 shows the difference of DOS between the SCAN and PBE+ U DFT results for a smaller 320-atom supercell of PM cubic phase SrVO₃. It can be seen from Figure 13 that the PBE+ U and SCAN functionals give (1) very similar DOS at Fermi level, and (2) very similar bandwidths; they, therefore, should predict very similar mass enhancement factors. (iii) The s - p bonded halide CsPbI₃ has been calculated using the PBE functional. Note that no spin-orbit coupling (SOC) has been considered for CsPbI₃ in this work because the PBE functional will give too small gap (~ 0.1 eV) if implied together with SOC; a better agreement with experimentally observed gap can be achieved by using SOC with a hybrid functional such as HSE, which is however beyond the scope of this work. (iv) The s - p bonded oxide SrBiO₃ has been calculated using the PBE with spin-orbit coupling effect.

For each compound, we have applied the DFT lattice constants obtained from the minimal cell model to all supercell calculations: $a=3.83$ Å (cubic SrVO₃), $a=6.27$ Å (cubic CsPbI₃), $a=5.51$ Å $b=5.81$ Å and $c=7.64$ Å (LaMnO₃ with Jahn-Teller-like distortion), $a=5.57$ Å and $c=7.87$ Å (LaMnO₃ without Jahn-Teller distortion), $a=6.01$ Å $b=6.20$ Å and $c=10.49$ Å (monoclinic SrBiO₃), $a=4.52$ Å (cubic SrBiO₃), $a=3.91$ Å (cubic SrTiO₃), and $a=4.03$ Å (cubic BaTiO₃). To minimize the numerical error, for all cells of the same compound in the same phase (*e.g.*, SrVO₃ single-f.u. cubic primitive cell vs. SrVO₃ 64-f.u. cubic supercell), their total energies are calculated using an uniformed energy cutoff for the plane-wave basis set, an uniformed tolerance for total energy convergence (10^{-8} eV/atom), and an *equivalent set of k -point* sampling in BZ for every cell (equivalent to a $12\times 12\times 12$ Γ -centered k -mesh in the primitive BZ).

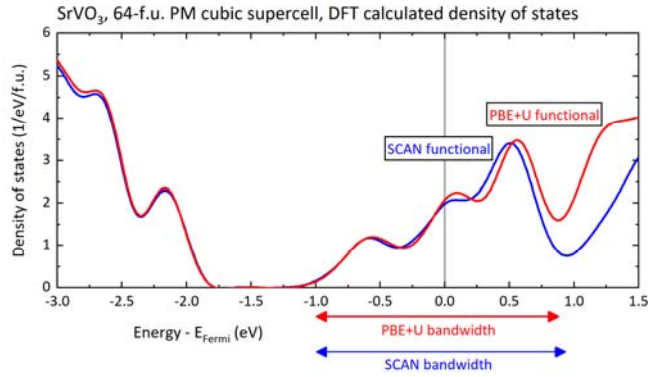


Figure 13 (1 column) | Comparison of DOS from DFT calculations using PBE+U (red curve) and SCAN (blue curve) functionals for the 64-f.u. (320-atom) PM cubic supercell of SrVO₃. The two functionals show remarkably similar DOS at Fermi level and very similar bandwidths (denoted by the red and blue arrows).

Appendix B: Magnetic structure of SrVO₃.

Table II summarizes the DFT total energies of different magnetic orders of cubic SrVO₃: NM – nonmagnetic, FM – ferromagnetic, AFM-G – G-type antiferromagnetic, AFM-A – A-type antiferromagnetic, and PM – collinear paramagnetic phase from SQS method. All magnetic structures show significant energy lowering than the nonmagnetic model, but very similar total energy with each other. The results agree with the experimental observation that SrVO₃ shows no magnetic order down to T=0 K.

Table II | Summary of DFT total energy for different collinear magnetic structures of cubic SrVO₃. The same PBE+U method has been applied for all SrVO₃ calculations. All structures have the same lattice constant and atomic positions and only differ in the way how up and down spin moments occupy vanadium sites. Magnetic orders NM, FM, AFM (G-type and A-type), and PM denote nonmagnetic, ferromagnetic, antiferromagnetic and paramagnetic (from SQS method), respectively. The DFT total energy of the NM phase has been chosen as the reference (0 eV).

Cubic SrVO ₃ magnetic phase	Total energy (meV/f.u.)
NM (1 f.u.)	0 (reference)
FM (1 f.u.)	-15
AFM-G (8 f.u.)	-31
AFM-A (2 f.u.)	-26

PM (64 f.u.)	-30
PM (128 f.u.)	-31

References

- [1] C. Kittel, *Introduction to Solid State Physics* (Wiley, 1966).
- [2] M. Yi, Y. Zhang, Z.-X. Shen, and D. Lu, *Role of the Orbital Degree of Freedom in Iron-Based Superconductors*, Npj Quantum Mater. **2**, 57 (2017).
- [3] Y. S. Kushnirenko, A. A. Kordyuk, A. V. Fedorov, E. Haubold, T. Wolf, B. Büchner, and S. V. Borisenko, *Anomalous Temperature Evolution of the Electronic Structure of FeSe*, Phys. Rev. B **96**, 100504 (2017).
- [4] M. Schlipf, S. Poncé, and F. Giustino, *Carrier Lifetimes and Polaronic Mass Enhancement in the Hybrid Halide Perovskite $\text{CH}_3\text{NH}_3\text{PbI}_3$ from Multiphonon Fröhlich Coupling*, Phys. Rev. Lett. **121**, 086402 (2018).
- [5] C. Verdi, F. Caruso, and F. Giustino, *Origin of the Crossover from Polarons to Fermi Liquids in Transition Metal Oxides*, Nat. Commun. **8**, 1 (2017).
- [6] Y. Okada, T. Arima, Y. Tokura, C. Murayama, and N. Mōri, *Doping- and Pressure-Induced Change of Electrical and Magnetic Properties in the Mott-Hubbard Insulator LaTiO_3* , Phys. Rev. B **48**, 9677 (1993).
- [7] J.-J. Zhou, O. Hellman, and M. Bernardi, *Electron-Phonon Scattering in the Presence of Soft Modes and Electron Mobility in SrTiO_3 Perovskite from First Principles*, Phys. Rev. Lett. **121**, 226603 (2018).
- [8] D. E. Shai, C. Adamo, D. W. Shen, C. M. Brooks, J. W. Harter, E. J. Monkman, B. Burganov, D. G. Schlom, and K. M. Shen, *Quasiparticle Mass Enhancement and Temperature Dependence of the Electronic Structure of Ferromagnetic SrRuO_3 Thin Films*, Phys. Rev. Lett. **110**, 087004 (2013).
- [9] T. M. Rice and M. Sigrist, *Sr_2RuO_4 : An Electronic Analogue of 3He ?*, J. Phys. Condens. Matter **7**, L643 (1995).
- [10] P. B. Allen, H. Berger, O. Chauvet, L. Forro, T. Jarlborg, A. Junod, B. Revaz, and G. Santi, *Transport Properties, Thermodynamic Properties, and Electronic Structure of SrRuO_3* , Phys. Rev. B **53**, 4393 (1996).
- [11] I. H. Inoue, O. Goto, H. Makino, N. E. Hussey, and M. Ishikawa, *Bandwidth Control in a Perovskite-Type $3d^1$ -Correlated Metal $\text{Ca}_{1-x}\text{Sr}_x\text{VO}_3$ I. Evolution of the Electronic Properties and Effective Mass*, Phys. Rev. B **58**, 4372 (1998).

- [12] T. Yoshida, M. Hashimoto, T. Takizawa, A. Fujimori, M. Kubota, K. Ono, and H. Eisaki, *Mass Renormalization in the Bandwidth-Controlled Mott-Hubbard Systems $SrVO_3$ and $CaVO_3$ Studied by Angle-Resolved Photoemission Spectroscopy*, Phys. Rev. B **82**, 085119 (2010).
- [13] T. Yoshida, K. Tanaka, H. Yagi, A. Ino, H. Eisaki, A. Fujimori, and Z.-X. Shen, *Direct Observation of the Mass Renormalization in $SrVO_3$ by Angle Resolved Photoemission Spectroscopy*, Phys. Rev. Lett. **95**, 146404 (2005).
- [14] T. Yoshida, M. Kobayashi, K. Yoshimatsu, H. Kumigashira, and A. Fujimori, *Correlated Electronic States of $SrVO_3$ Revealed by Angle-Resolved Photoemission Spectroscopy*, J. Electron Spectrosc. Relat. Phenom. **208**, 11 (2016).
- [15] I. A. Nekrasov, K. Held, G. Keller, D. E. Kondakov, Th. Pruschke, M. Kollar, O. K. Andersen, V. I. Anisimov, and D. Vollhardt, *Momentum-Resolved Spectral Functions of $SrVO_3$ Calculated by LDA+DMFT*, Phys. Rev. B **73**, 155112 (2006).
- [16] J. M. Tomczak, M. Casula, T. Miyake, and S. Biermann, *Asymmetry in Band Widening and Quasiparticle Lifetimes in $SrVO_3$: Competition between Screened Exchange and Local Correlations from Combined GW and Dynamical Mean-Field Theory GW+DMFT*, Phys. Rev. B **90**, 165138 (2014).
- [17] R. Sakuma, Ph. Werner, and F. Aryasetiawan, *Electronic Structure of $SrVO_3$ within GW+DMFT*, Phys. Rev. B **88**, 235110 (2013).
- [18] E. Pavarini, S. Biermann, A. Poteryaev, A. I. Lichtenstein, A. Georges, and O. K. Andersen, *Mott Transition and Suppression of Orbital Fluctuations in Orthorhombic $3d^1$ Perovskites*, Phys. Rev. Lett. **92**, 176403 (2004).
- [19] X. Deng, K. Haule, and G. Kotliar, *Transport Properties of Metallic Ruthenates: A DFT+DMFT Investigation*, Phys. Rev. Lett. **116**, 256401 (2016).
- [20] E. Jakobi, S. Kanungo, S. Sarkar, S. Schmitt, and T. Saha-Dasgupta, *LDA+DMFT Study of Ru-Based Perovskite $SrRuO_3$ and $CaRuO_3$* , Phys. Rev. B **83**, 041103 (2011).
- [21] S. L. Skornyakov, N. A. Skorikov, A. V. Lukoyanov, A. O. Shorikov, and V. I. Anisimov, *LDA+DMFT Spectral Functions and Effective Electron Mass Enhancement in the Superconductor $LaFePO$* , Phys. Rev. B **81**, 174522 (2010).
- [22] E. A. Nowadnick, J. P. Ruf, H. Park, P. D. C. King, D. G. Schlom, K. M. Shen, and A. J. Millis, *Quantifying Electronic Correlation Strength in a Complex Oxide: A Combined DMFT and ARPES Study of $LaNiO_3$* , Phys. Rev. B **92**, 245109 (2015).
- [23] Z. P. Yin, K. Haule, and G. Kotliar, *Kinetic Frustration and the Nature of the Magnetic and Paramagnetic States in Iron Pnictides and Iron Chalcogenides*, Nat. Mater. **10**, 932 (2011).
- [24] J. Mravlje, M. Aichhorn, T. Miyake, K. Haule, G. Kotliar, and A. Georges, *Coherence-Incoherence Crossover and the Mass-Renormalization Puzzles in Sr_2RuO_4* , Phys. Rev. Lett. **106**, 096401 (2011).
- [25] J. M. Tomczak, M. van Schilfgaarde, and G. Kotliar, *Many-Body Effects in Iron Pnictides and Chalcogenides: Nonlocal Versus Dynamic Origin of Effective Masses*, Phys. Rev. Lett. **109**, 237010 (2012).

- [26] G. Trimarchi, Z. Wang, and A. Zunger, *Polymorphous Band Structure Model of Gapping in the Antiferromagnetic and Paramagnetic Phases of the Mott Insulators MnO, FeO, CoO, and NiO*, Phys. Rev. B **97**, 035107 (2018).
- [27] J. Varignon, M. Bibes, and A. Zunger, *Origin of Band Gaps in 3d Perovskite Oxides*, Nat. Commun. **10**, 1658 (2019).
- [28] O. I. Malyi, G. M. Dalpian, X.-G. Zhao, Z. Wang, and A. Zunger, *Realization of Predicted Exotic Materials: The Burden of Proof*, Mater. Today **32**, 35 (2020).
- [29] O. I. Malyi and A. Zunger, *False Metals, Real Insulators, and Degenerate Gapped Metals*, Appl. Phys. Rev. **7**, 041310 (2020).
- [30] M. R. Filip, G. E. Eperon, H. J. Snaith, and F. Giustino, *Steric Engineering of Metal-Halide Perovskites with Tunable Optical Band Gaps*, Nat. Commun. **5**, 1 (2014).
- [31] J. Even and C. Katan, *Ab Initio and First Principles Studies of Halide Perovskites*, Halide Perovskites Photovolt. Light Emit. Devices Beyond 25 (2018).
- [32] D. H. Fabini, G. Laurita, J. S. Bechtel, C. C. Stoumpos, H. A. Evans, A. G. Kontos, Y. S. Raptis, P. Falaras, A. Van der Ven, and M. G. Kanatzidis, *Dynamic Stereochemical Activity of the Sn²⁺ Lone Pair in Perovskite CsSnBr₃*, J. Am. Chem. Soc. **138**, 11820 (2016).
- [33] S. Chakraborty, W. Xie, N. Mathews, M. Sherburne, R. Ahuja, M. Asta, and S. G. Mhaisalkar, *Rational Design: A High-Throughput Computational Screening and Experimental Validation Methodology for Lead-Free and Emergent Hybrid Perovskites*, ACS Energy Lett. **2**, 837 (2017).
- [34] E. S. Božin, C. D. Malliakas, P. Souvatzis, T. Proffen, N. A. Spaldin, M. G. Kanatzidis, and S. J. L. Billinge, *Entropically Stabilized Local Dipole Formation in Lead Chalcogenides*, Science **330**, 1660 (2010).
- [35] A. N. Beecher, O. E. Semonin, J. M. Skelton, J. M. Frost, M. W. Terban, H. Zhai, A. Alatas, J. S. Owen, A. Walsh, and S. J. L. Billinge, *Direct Observation of Dynamic Symmetry Breaking above Room Temperature in Methylammonium Lead Iodide Perovskite*, ACS Energy Lett. **1**, 880 (2016).
- [36] X. Zhao, G. M. Dalpian, Z. Wang, and A. Zunger, *Polymorphous Nature of Cubic Halide Perovskites*, Phys. Rev. B **101**, 155137 (2020).
- [37] I.-K. Jeong, T. W. Darling, J. K. Lee, Th. Proffen, R. H. Heffner, J. S. Park, K. S. Hong, W. Dmowski, and T. Egami, *Direct Observation of the Formation of Polar Nanoregions in Pb(Mg_{1/3}Nb_{2/3})O₃ Using Neutron Pair Distribution Function Analysis*, Phys. Rev. Lett. **94**, 147602 (2005).
- [38] E. S. Bozin, W. G. Yin, R. J. Koch, M. Abeykoon, Y. S. Hor, H. Zheng, H. C. Lei, C. Petrovic, J. F. Mitchell, and S. J. L. Billinge, *Local Orbital Degeneracy Lifting as a Precursor to an Orbital-Selective Peierls Transition*, Nat. Commun. **10**, 1 (2019).
- [39] T. Egami and S. J. Billinge, *Underneath the Bragg Peaks: Structural Analysis of Complex Materials - 2nd Edition* (Elsevier, 2012).
- [40] J. J. Rehr and R. C. Albers, *Theoretical Approaches to X-Ray Absorption Fine Structure*, Rev. Mod. Phys. **72**, 621 (2000).

- [41] J. C. Mikkelsen Jr and J. B. Boyce, *Atomic-Scale Structure of Random Solid Solutions: Extended X-Ray-Absorption Fine-Structure Study of Ga_{1-x}In_xAs*, Phys. Rev. Lett. **49**, 1412 (1982).
- [42] A. Bianconi, N. L. Saini, A. Lanzara, M. Missori, T. Rossetti, H. Oyanagi, H. Yamaguchi, K. Oka, and T. Ito, *Determination of the Local Lattice Distortions in the CuO₂ Plane of La_{1.85}Sr_{0.15}CuO₄*, Phys. Rev. Lett. **76**, 3412 (1996).
- [43] A. M. Glazer, *The Classification of Tilted Octahedra in Perovskites*, Acta Crystallogr. B **28**, 3384 (1972).
- [44] Q. Zhang, T. Cagin, and W. A. Goddard, *The Ferroelectric and Cubic Phases in BaTiO₃ Ferroelectrics Are Also Antiferroelectric*, Proc. Natl. Acad. Sci. **103**, 14695 (2006).
- [45] J. A. Alonso, J. L. García-Muñoz, M. T. Fernández-Díaz, M. A. G. Aranda, M. J. Martínez-Lope, and M. T. Casais, *Charge Disproportionation in RNiO₃ Perovskites: Simultaneous Metal-Insulator and Structural Transition in YNiO₃*, Phys. Rev. Lett. **82**, 3871 (1999).
- [46] J. A. Alonso, M. J. Martínez-Lope, M. T. Casais, and M. T. Fernández-Díaz, *Evolution of the Jahn–Teller Distortion of MnO₆ Octahedra in RMnO₃ Perovskites (R = Pr, Nd, Dy, Tb, Ho, Er, Y): A Neutron Diffraction Study*, Inorg. Chem. **39**, 917 (2000).
- [47] R. Prasanna, A. Gold-Parker, T. Leijtens, B. Conings, A. Babayigit, H.-G. Boyen, M. F. Toney, and M. D. McGehee, *Band Gap Tuning via Lattice Contraction and Octahedral Tilting in Perovskite Materials for Photovoltaics*, J. Am. Chem. Soc. **139**, 11117 (2017).
- [48] Z. Gui, L.-W. Wang, and L. Bellaiche, *Electronic Properties of Electrical Vortices in Ferroelectric Nanocomposites from Large-Scale Ab Initio Computations*, Nano Lett. **15**, 3224 (2015).
- [49] K. Foyevtsova, A. Khazraie, I. Elfimov, and G. A. Sawatzky, *Hybridization Effects and Bond Disproportionation in the Bismuth Perovskites*, Phys. Rev. B **91**, 121114 (2015).
- [50] N. Balke, B. Winchester, W. Ren, Y. H. Chu, A. N. Morozovska, E. A. Eliseev, M. Huijben, R. K. Vasudevan, P. Maksymovych, J. Britson, S. Jesse, I. Kornev, R. Ramesh, L. Bellaiche, L. Q. Chen, and S. V. Kalinin, *Enhanced Electric Conductivity at Ferroelectric Vortex Cores in BiFeO₃*, Nat. Phys. **8**, 1 (2012).
- [51] A. Mercy, J. Bieder, J. Íñiguez, and P. Ghosez, *Structurally Triggered Metal-Insulator Transition in Rare-Earth Nickelates*, Nat. Commun. **8**, 1 (2017).
- [52] A. Amat, E. Mosconi, E. Ronca, C. Quarti, P. Umari, Md. K. Nazeeruddin, M. Grätzel, and F. De Angelis, *Cation-Induced Band-Gap Tuning in Organohalide Perovskites: Interplay of Spin–Orbit Coupling and Octahedra Tilting*, Nano Lett. **14**, 3608 (2014).
- [53] I. Leonov, Dm. Korotin, N. Binggeli, V. I. Anisimov, and D. Vollhardt, *Computation of Correlation-Induced Atomic Displacements and Structural Transformations in Paramagnetic KCuF₃ and LaMnO₃*, Phys. Rev. B **81**, 075109 (2010).
- [54] X. Wang, M. J. Han, L. de’ Medici, H. Park, C. A. Marianetti, and A. J. Millis, *Covalency, Double-Counting, and the Metal-Insulator Phase Diagram in Transition Metal Oxides*, Phys. Rev. B **86**, 195136 (2012).

- [55] M. De Raychaudhury, E. Pavarini, and O. K. Andersen, *Orbital Fluctuations in the Different Phases of $LaVO_3$ and YVO_3* , Phys. Rev. Lett. **99**, 126402 (2007).
- [56] Z. Wang, J.-W. Luo, and A. Zunger, *Alloy Theory with Atomic Resolution for Rashba or Topological Systems*, Phys. Rev. Mater. **3**, 044605 (2019).
- [57] Z. Wang, Q. Liu, J.-W. Luo, and A. Zunger, *Digging for Topological Property in Disordered Alloys: The Emergence of Weyl Semimetal Phase and Sequential Band Inversions in $PbSe-SnSe$ Alloys*, Mater. Horiz. (2019).
- [58] Z. Wang, X.-G. Zhao, R. Koch, S. J. L. Billinge, and A. Zunger, *Understanding Electronic Peculiarities in Tetragonal $FeSe$ as Local Structural Symmetry Breaking*, Phys. Rev. B **102**, 235121 (2020).
- [59] J. P. Perdew and A. Zunger, *Self-Interaction Correction to Density-Functional Approximations for Many-Electron Systems*, Phys. Rev. B **23**, 5048 (1981).
- [60] P. S. Bagus and H. F. Schaefer III, *Localized and Delocalized $1s$ Hole States of the O_2^+ Molecular Ion*, J. Chem. Phys. **56**, 224 (1972).
- [61] O. Gunnarsson and B. I. Lundqvist, *Exchange and Correlation in Atoms, Molecules, and Solids by the Spin-Density-Functional Formalism*, Phys. Rev. B **13**, 4274 (1976).
- [62] M. R. Pederson, R. A. Heaton, and C. C. Lin, *Density-functional Theory with Self-interaction Correction: Application to the Lithium Molecule*, J. Chem. Phys. **82**, 2688 (1985).
- [63] J. P. Perdew, A. Ruzsinszky, J. Sun, N. K. Nepal, and A. D. Kaplan, *Interpretations of Ground-State Symmetry Breaking and Strong Correlation in Wavefunction and Density Functional Theories*, Proc. Natl. Acad. Sci. **118**, (2021).
- [64] C. Yannouleas and U. Landman, *Electronic Shell Effects in Triaxially Deformed Metal Clusters: A Systematic Interpretation of Experimental Observations*, Phys. Rev. B **51**, 1902 (1995).
- [65] F. HERMAN, *Theoretical Investigation of the Electronic Energy Band Structure of Solids*, Rev. Mod. Phys. **30**, 102 (1958).
- [66] P. Yu and M. Cardona, *2.6: The $k p$ Method of Band-Structure Calculations*, in *Fundamentals of Semiconductors: Physics and Materials Properties*, 3rd ed. (Springer-Verlag Berlin Heidelberg, 1996).
- [67] A. J. Cohen, P. Mori-Sánchez, and W. Yang, *Fractional Charge Perspective on the Band Gap in Density-Functional Theory*, Phys. Rev. B **77**, 115123 (2008).
- [68] P. Mori-Sánchez, A. J. Cohen, and W. Yang, *Localization and Delocalization Errors in Density Functional Theory and Implications for Band-Gap Prediction*, Phys. Rev. Lett. **100**, 146401 (2008).
- [69] J. P. Perdew, W. Yang, K. Burke, Z. Yang, E. K. Gross, M. Scheffler, G. E. Scuseria, T. M. Henderson, I. Y. Zhang, and A. Ruzsinszky, *Understanding Band Gaps of Solids in Generalized Kohn-Sham Theory*, Proc. Natl. Acad. Sci. **114**, 2801 (2017).
- [70] A. H. Hill, C. L. Kennedy, E. S. Massaro, and E. M. Grumstrup, *Perovskite Carrier Transport: Disentangling the Impacts of Effective Mass and Scattering Time Through Microscopic Optical Detection*, J. Phys. Chem. Lett. **9**, 2808 (2018).

- [71] M. Takizawa, M. Minohara, H. Kumigashira, D. Toyota, M. Oshima, H. Wadati, T. Yoshida, A. Fujimori, M. Lippmaa, M. Kawasaki, H. Koinuma, G. Sordi, and M. Rozenberg, *Coherent and Incoherent d Band Dispersions in SrVO₃*, Phys. Rev. B **80**, 235104 (2009).
- [72] A. Chikamatsu, H. Wadati, H. Kumigashira, M. Oshima, A. Fujimori, N. Hamada, T. Ohnishi, M. Lippmaa, K. Ono, and M. Kawasaki, *Band Structure and Fermi Surface of La_{0.6}Sr_{0.4}MnO₃ Thin Films Studied by in Situ Angle-Resolved Photoemission Spectroscopy*, Phys. Rev. B **73**, 195105 (2006).
- [73] J. L. M. van Mechelen, D. van der Marel, C. Grimaldi, A. B. Kuzmenko, N. P. Armitage, N. Reyren, H. Hagemann, and I. I. Mazin, *Electron-Phonon Interaction and Charge Carrier Mass Enhancement in SrTiO₃*, Phys. Rev. Lett. **100**, 226403 (2008).
- [74] L.-W. Wang, L. Bellaiche, S.-H. Wei, and A. Zunger, “Majority Representation” of Alloy Electronic States, Phys. Rev. Lett. **80**, 4725 (1998).
- [75] V. Popescu and A. Zunger, *Effective Band Structure of Random Alloys*, Phys. Rev. Lett. **104**, 236403 (2010).
- [76] V. Popescu and A. Zunger, *Extracting E versus k Effective Band Structure from Supercell Calculations on Alloys and Impurities*, Phys. Rev. B **85**, 085201 (2012).
- [77] A. Zunger, S.-H. Wei, L. G. Ferreira, and J. E. Bernard, *Special Quasirandom Structures*, Phys. Rev. Lett. **65**, 353 (1990).
- [78] L. Bellaiche and A. Zunger, *Effects of Atomic Short-Range Order on the Electronic and Optical Properties of GaAsN, GaInN, and GaInAs Alloys*, Phys. Rev. B **57**, 4425 (1998).
- [79] C. Wolverton, V. Ozolins, and A. Zunger, *Short-Range-Order Types in Binary Alloys: A Reflection of Coherent Phase Stability*, J. Phys. Condens. Matter **12**, 2749 (2000).
- [80] B. L. Chamberland and P. S. Danielson, *Alkaline-Earth Vanadium (IV) Oxides Having the AVO₃ Composition*, J. Solid State Chem. **3**, 243 (1971).
- [81] M. J. Rey, Ph. Dehaut, J. C. Joubert, B. Lambert-Andron, M. Cyrot, and F. Cyrot-Lackmann, *Preparation and Structure of the Compounds SrVO₃ and Sr₂VO₄*, J. Solid State Chem. **86**, 101 (1990).
- [82] P. Puschnig and D. Lüftner, *Simulation of Angle-Resolved Photoemission Spectra by Approximating the Final State by a Plane Wave: From Graphene to Polycyclic Aromatic Hydrocarbon Molecules*, J. Electron Spectrosc. Relat. Phenom. **200**, 193 (2015).
- [83] S. Moser, *An Experimentalist’s Guide to the Matrix Element in Angle Resolved Photoemission*, J. Electron Spectrosc. Relat. Phenom. **214**, 29 (2017).
- [84] D. E. Eastman, J. A. Knapp, and F. J. Himpsel, *Direct Determination of Lifetime and Energy Dispersion for the Empty Δ₁ Conduction Band of Copper*, Phys. Rev. Lett. **41**, 825 (1978).
- [85] J. A. Knapp, F. J. Himpsel, and D. E. Eastman, *Experimental Energy Band Dispersions and Lifetimes for Valence and Conduction Bands of Copper Using Angle-Resolved Photoemission*, Phys. Rev. B **19**, 4952 (1979).

- [86] I. Stockem, A. Bergman, A. Glensk, T. Hickel, F. Körmann, B. Grabowski, J. Neugebauer, and B. Alling, *Anomalous Phonon Lifetime Shortening in Paramagnetic CrN Caused by Spin-Lattice Coupling: A Combined Spin and Ab Initio Molecular Dynamics Study*, Phys. Rev. Lett. **121**, 125902 (2018).
- [87] V. M. Goldschmidt, *Die Gesetze der Krystallochemie*, Naturwissenschaften **14**, 477 (1926).
- [88] X. Qiu, Th. Proffen, J. F. Mitchell, and S. J. L. Billinge, *Orbital Correlations in the Pseudocubic O and Rhombohedral R Phases of LaMnO₃*, Phys. Rev. Lett. **94**, 177203 (2005).
- [89] P. García-Fernández, S. Ghosh, N. J. English, and J. A. Aramburu, *Benchmark Study for the Application of Density Functional Theory to the Prediction of Octahedral Tilting in Perovskites*, Phys. Rev. B **86**, 144107 (2012).
- [90] J. Even, L. Pedesseau, J.-M. Jancu, and C. Katan, *DFT and $k \cdot p$ Modelling of the Phase Transitions of Lead and Tin Halide Perovskites for Photovoltaic Cells*, Phys. Status Solidi RRL – Rapid Res. Lett. **8**, 31 (2014).
- [91] E. Mosconi, P. Umari, and F. D. Angelis, *Electronic and Optical Properties of MAPbX₃ Perovskites (X = I, Br, Cl): A Unified DFT and GW Theoretical Analysis*, Phys. Chem. Chem. Phys. **18**, 27158 (2016).
- [92] A. Perrichon, E. Jedvik Granhed, G. Romanelli, A. Piovano, A. Lindman, P. Hyldgaard, G. Wahnström, and M. Karlsson, *Unraveling the Ground-State Structure of BaZrO₃ by Neutron Scattering Experiments and First-Principles Calculations*, Chem. Mater. **32**, 2824 (2020).
- [93] Z. Xiao, W. Meng, J. Wang, D. B. Mitzi, and Y. Yan, *Searching for Promising New Perovskite-Based Photovoltaic Absorbers: The Importance of Electronic Dimensionality*, Mater. Horiz. **4**, 206 (2017).
- [94] S. C. Miller and W. F. Love, *Tables of Irreducible Representations of Space Groups and Co-Representations of Magnetic Space Groups* (Pruett Press, 1967).
- [95] E. Pavarini and E. Koch, *Origin of Jahn-Teller Distortion and Orbital Order in LaMnO₃*, Phys. Rev. Lett. **104**, 086402 (2010).
- [96] S. Satpathy, Z. S. Popović, and F. R. Vukajlović, *Electronic Structure of the Perovskite Oxides: La_{1-x}Ca_xMnO₃*, Phys. Rev. Lett. **76**, 960 (1996).
- [97] J. H. Lee, K. T. Delaney, E. Bousquet, N. A. Spaldin, and K. M. Rabe, *Strong Coupling of Jahn-Teller Distortion to Oxygen-Octahedron Rotation and Functional Properties in Epitaxially Strained Orthorhombic LaMnO₃*, Phys. Rev. B **88**, 174426 (2013).
- [98] T. A. Mellan, F. Cora, R. Grau-Crespo, and S. Ismail-Beigi, *Importance of Anisotropic Coulomb Interaction in LaMnO₃*, Phys. Rev. B **92**, 085151 (2015).
- [99] J. Varignon, M. Bibes, and A. Zunger, *Mott Gapping in 3d ABO₃ Perovskites without Mott-Hubbard Interelectronic Repulsion Energy U*, Phys. Rev. B **100**, 035119 (2019).
- [100] J. Varignon, M. Bibes, and A. Zunger, *Origins versus Fingerprints of the Jahn-Teller Effect in d-Electron ABX₃ Perovskites*, Phys. Rev. Res. **1**, 033131 (2019).
- [101] J. B. Goodenough, *Jahn-Teller Phenomena in Solids*, Annu. Rev. Mater. Sci. **28**, 1 (1998).

- [102] J. Kuneš, I. Leonov, M. Kollar, K. Byczuk, V. I. Anisimov, and D. Vollhardt, *Dynamical Mean-Field Approach to Materials with Strong Electronic Correlations*, Eur. Phys. J. Spec. Top. **180**, 5 (2009).
- [103] H. Banerjee, O. Janson, K. Held, and T. Saha-Dasgupta, *Electronic and Magnetic State of LaMnO_3 Epitaxially Strained on SrTiO_3 : Effect of Local Correlation and Nonlocal Exchange*, Phys. Rev. B **100**, 115143 (2019).
- [104] P. V. Balachandran and J. M. Rondinelli, *Interplay of Octahedral Rotations and Breathing Distortions in Charge-Ordering Perovskite Oxides*, Phys. Rev. B **88**, 054101 (2013).
- [105] G. M. Dalpian, Q. Liu, J. Varignon, M. Bibes, and A. Zunger, *Bond Disproportionation, Charge Self-Regulation, and Ligand Holes in s - p and in d -Electron ABX_3 Perovskites by Density Functional Theory*, Phys. Rev. B **98**, 075135 (2018).
- [106] S. M. Kazakov, C. Chailout, P. Bordet, J. J. Capponi, M. Nunez-Regueiro, A. Rysak, J. L. Tholence, P. G. Radaelli, S. N. Putilin, and E. V. Antipov, *Discovery of a Second Family of Bismuth-Oxide-Based Superconductors*, Nature **390**, 6656 (1997).
- [107] K. Tsuda and M. Tanaka, *Refinement of Crystal Structure Parameters Using Convergent-Beam Electron Diffraction: The Low-Temperature Phase of SrTiO_3* , Acta Crystallogr. A **51**, 7 (1995).
- [108] Yu. A. Abramov, V. G. Tsirel'son, V. E. Zavodnik, S. A. Ivanov, and I. D. Brown, *The Chemical Bond and Atomic Displacements in SrTiO_3 from x -Ray Diffraction Analysis*, Acta Crystallogr. B **51**, 942 (1995).
- [109] K. B. Lyons and P. A. Fleury, *Phonon Interactions and the Dynamic Central Peak in SrTiO_3 near the Structural Phase Transition*, Solid State Commun. **23**, 477 (1977).
- [110] A. van Roekeghem and S. Biermann, *Screened Exchange Dynamical Mean-Field Theory and Its Relation to Density Functional Theory: SrVO_3 and SrTiO_3* , EPL Europhys. Lett. **108**, 57003 (2014).
- [111] A. F. Santander-Syro, O. Copie, T. Kondo, F. Fortuna, S. Pailhès, R. Weht, X. G. Qiu, F. Bertran, A. Nicolaou, A. Taleb-Ibrahimi, P. Le Fèvre, G. Herranz, M. Bibes, N. Reyren, Y. Apertet, P. Lecoeur, A. Barthélémy, and M. J. Rozenberg, *Two-Dimensional Electron Gas with Universal Subbands at the Surface of SrTiO_3* , Nature **469**, 7329 (2011).
- [112] Y. J. Chang, A. Bostwick, Y. S. Kim, K. Horn, and E. Rotenberg, *Structure and Correlation Effects in Semiconducting SrTiO_3* , Phys. Rev. B **81**, 235109 (2010).
- [113] W. Zhong and D. Vanderbilt, *Competing Structural Instabilities in Cubic Perovskites*, Phys. Rev. Lett. **74**, 2587 (1995).
- [114] R. F. Berger, C. J. Fennie, and J. B. Neaton, *Band Gap and Edge Engineering via Ferroic Distortion and Anisotropic Strain: The Case of SrTiO_3* , Phys. Rev. Lett. **107**, 146804 (2011).
- [115] J. H. Haeni, P. Irvin, W. Chang, R. Uecker, P. Reiche, Y. L. Li, S. Choudhury, W. Tian, M. E. Hawley, and B. Craigo, *Room-Temperature Ferroelectricity in Strained SrTiO_3* , Nature **430**, 758 (2004).
- [116] T. F. Nova, A. S. Disa, M. Fechner, and A. Cavalleri, *Metastable Ferroelectricity in Optically Strained SrTiO_3* , Science **364**, 1075 (2019).

- [117] A. Janotti, J. B. Varley, M. Choi, and C. G. Van de Walle, *Vacancies and Small Polarons in SrTiO₃*, Phys. Rev. B **90**, 085202 (2014).
- [118] X. Hao, Z. Wang, M. Schmid, U. Diebold, and C. Franchini, *Coexistence of Trapped and Free Excess Electrons in SrTiO₃*, Phys. Rev. B **91**, 085204 (2015).
- [119] E. Bousquet, M. Dawber, N. Stucki, C. Lichtensteiger, P. Hermet, S. Gariglio, J.-M. Triscone, and P. Ghosez, *Improper Ferroelectricity in Perovskite Oxide Artificial Superlattices*, Nature **452**, 732 (2008).
- [120] M. Zacharias, M. Scheffler, and C. Carbogno, *Fully Anharmonic Nonperturbative Theory of Vibronically Renormalized Electronic Band Structures*, Phys. Rev. B **102**, 045126 (2020).
- [121] Y. Aiura, I. Hase, H. Bando, T. Yasue, T. Saitoh, and D. S. Dessau, *Photoemission Study of the Metallic State of Lightly Electron-Doped SrTiO₃*, Surf. Sci. **515**, 61 (2002).
- [122] S. A. Chambers, Y. Du, Z. Zhu, J. Wang, M. J. Wahila, L. F. J. Piper, A. Prakash, J. Yue, B. Jalan, S. R. Spurgeon, D. M. Kepaptsoglou, Q. M. Ramasse, and P. V. Sushko, *Interconversion of Intrinsic Defects in SrTiO₃ (001)*, Phys. Rev. B **97**, 245204 (2018).
- [123] A. Fujimori, I. Hase, M. Nakamura, H. Namatame, Y. Fujishima, Y. Tokura, M. Abbate, F. M. F. de Groot, M. T. Czyzyk, J. C. Fuggle, O. Strebel, F. Lopez, M. Domke, and G. Kaindl, *Doping-Induced Changes in the Electronic Structure of La_xSr_{1-x}TiO₃: Limitation of the One-Electron Rigid-Band Model and the Hubbard Model*, Phys. Rev. B **46**, 9841 (1992).
- [124] Y.-T. Chi, M. Youssef, L. Sun, K. J. Van Vliet, and B. Yildiz, *Accessible Switching of Electronic Defect Type in SrTiO₃ via Biaxial Strain*, Phys. Rev. Mater. **2**, 055801 (2018).
- [125] L. Rimai, J. L. Parsons, J. T. Hickmott, and T. Nakamura, *Raman Spectrum of Long-Wavelength Phonons in Tetragonal Barium Titanate*, Phys. Rev. **168**, 623 (1968).
- [126] J. L. Parsons and L. Rimai, *Raman Spectrum of BaTiO₃*, Solid State Commun. **5**, 423 (1967).
- [127] A. M. Quittet and M. Lambert, *Temperature Dependence of the Raman Cross Section and Light Absorption in Cubic BaTiO₃*, Solid State Commun. **12**, 1053 (1973).
- [128] F. Jona and G. Shirane, *Ferroelectric Crystals, International Series of Monographs on Solid State Physics* (Pergamon press, 1962).
- [129] H.-S. Lee, T. Mizoguchi, T. Yamamoto, S.-J. L. Kang, and Y. Ikuhara, *First-Principles Calculation of Defect Energetics in Cubic-BaTiO₃ and a Comparison with SrTiO₃*, Acta Mater. **55**, 6535 (2007).
- [130] Y. Xie, H. Yu, G. Zhang, and H. Fu, *Lattice Dynamics Investigation of Different Transition Behaviors of Cubic BaTiO₃ and SrTiO₃ by First-Principles Calculations*, J. Phys. Condens. Matter **20**, 215215 (2008).
- [131] V. Mishra, A. Sagdeo, V. Kumar, M. K. Warshi, H. M. Rai, S. K. Saxena, D. R. Roy, V. Mishra, R. Kumar, and P. R. Sagdeo, *Electronic and Optical Properties of BaTiO₃ across Tetragonal to Cubic Phase Transition: An Experimental and Theoretical Investigation*, J. Appl. Phys. **122**, 065105 (2017).

- [132] A. M. Pugachev, V. I. Kovalevskii, N. V. Surovtsev, S. Kojima, S. A. Prosandeev, I. P. Raevski, and S. I. Raevskaya, *Broken Local Symmetry in Paraelectric BaTiO₃ Proved by Second Harmonic Generation*, Phys. Rev. Lett. **108**, 247601 (2012).
- [133] H. B. Gray, *Molecular Orbital Theory for Transition Metal Complexes*, J. Chem. Educ. **41**, 2 (1964).
- [134] N. Tancogne-Dejean, F. G. Eich, and A. Rubio, *Time-Dependent Magnons from First Principles*, J. Chem. Theory Comput. **16**, 1007 (2020).
- [135] P. Steneteg, B. Alling, and I. A. Abrikosov, *Equation of State of Paramagnetic CrN from Ab Initio Molecular Dynamics*, Phys. Rev. B **85**, 144404 (2012).
- [136] F. Schmitt, P. S. Kirchmann, U. Bovensiepen, R. G. Moore, L. Rettig, M. Krenz, J.-H. Chu, N. Ru, L. Perfetti, and D. H. Lu, *Transient Electronic Structure and Melting of a Charge Density Wave in TbTe₃*, Science **321**, 1649 (2008).
- [137] G. Kresse and J. Furthmüller, *Efficiency of Ab-Initio Total Energy Calculations for Metals and Semiconductors Using a Plane-Wave Basis Set*, Comput. Mater. Sci. **6**, 15 (1996).
- [138] G. Kresse and J. Furthmüller, *Efficient Iterative Schemes for Ab Initio Total-Energy Calculations Using a Plane-Wave Basis Set*, Phys. Rev. B **54**, 11169 (1996).
- [139] J. Sun, A. Ruzsinszky, and J. P. Perdew, *Strongly Constrained and Appropriately Normed Semilocal Density Functional*, Phys. Rev. Lett. **115**, 036402 (2015).
- [140] C. Lane, J. W. Furness, I. G. Buda, Y. Zhang, R. S. Markiewicz, B. Barbiellini, J. Sun, and A. Bansil, *Antiferromagnetic Ground State of La₂CuO₄: A Parameter-Free Ab Initio Description*, Phys. Rev. B **98**, 125140 (2018).